INVERSE PROBLEM IN QUANTITATIVE SUSCEPTIBILITY MAPPING: NUMERICAL AND MACHINE LEARNING APPROACHES

A Dissertation

Presented to the Faculty of the Graduate School

of Cornell University

In Partial Fulfillment of the Requirements for the Degree of

Doctor of Philosophy

by

ZHE LIU

MAY 2019

INVERSE PROBLEM IN QUANTITATIVE SUSCEPTIBILITY MAPPING: NUMERICAL AND MACHINE LEARNING APPROACHES

ZHE LIU, PH. D.

Cornell University 2019

Magnetic susceptibility reflects the concentration of bio-metal elements such as iron, calcium or gadolinium, providing means to investigate diseases such as multiple sclerosis, Alzheimer's disease, hemorrhage and calcification. Numerous approaches have been proposed to provide magnetic susceptibility estimation from magnetic resonance imaging (MRI). While those methods are designed for specific body parts or pathologies, a unified framework is elusive from literature for reliable susceptibility estimation in both normal and pathological scenarios.

This thesis developed algorithms that improve the accuracy, robustness and applicability of quantitative susceptibility mapping (QSM) for both healthy and pathological subjects. First, a dedicated regularized model was proposed to enable automated zero reference for QSM using cerebrospinal fluid. Second, convolutional neural network was combined with numerical optimization for superior anatomical contrast in QSM reconstruction. Finally, a total field inversion approach was presented to enable QSM for both healthy subject and hemorrhage patient.

With the technical advances in this thesis, QSM requires less manual effort in susceptibility quantification, admits detailed recovery of anatomical structures and applies to both healthy subject and patient via a unified framework.

BIOGRAPHICAL SKETCH

Zhe Liu was born in Tianjin, China in 1991. He received the Bachelor of Engineering degree in Automation from Tsinghua University in 2013. He joined the graduate program in Biomedical Engineering at Cornell University in the Fall 2013, and received the Master of Science degree in Biomedical Engineering in 2016.

This thesis is dedicated to my parents,

who supported me through my difficult times

and always encouraged me to pursue what I love.

ACKNOWLEDGMENTS

During my Ph.D. study, I have always been grateful for the help and support of many people. Not only did they provide constructive ideas through scientific discussion and communication, but also gave moral support to my research and to my life in general.

First, I would like to thank my advisor and mentor, Prof. Yi Wang. His rigorous attitude towards scientific research constantly reminded me of the most important quality of a Ph.D.: critical thinking. I was always impressed by his insistence on a thorough understanding of things, which is extremely beneficial not only in my research but also in tackling every problem in my future career.

A large amount of thanks is owed to another professor, Dr. Pascal Spincemaille. He was the first person I would turn to whenever I encountered academic or technical hurdles in my research, and he was always patient, insightful and providing great suggestions. He also contributed a ton in our development of the online server solution for our institute which brought great advance to the clinical QSM implementation.

Although my research is focused on algorithms and technical advances, the insight from a clinical perspective is indispensable. Dr. Martin Prince, an expert from both medicine and physics worlds, provided great help in explaining to me various medical concepts and procedures, always identified the merits in a technical project and steered the discussion into a clinically profound direction. Dr. Shun Zhang, Dr. Yihao Yao and Dr. Yan Zhang contributed a lot helping me through the demanding tasks including ROI segmentation, in almost all my projects.

My research could never be achieved without the help of other colleagues in our lab. Dr. Thanh Nguyen walked me through the fundamentals of MRI pulse sequence

programming and provided constructive discussion with his expertise on MRI basics and applications. A former student, Tian Liu, taught me a lot on basic concepts of QSM and computer programming. I also want to thank Alexey Dimov, for his contribution in our collaborated UTE project and his support through many late-night scans. I am grateful to Youngwook Kee, who is an expert on maths and equations. We had countless long discussions on my research and his insightful comments finally constructed a significant part of my first publication. Kelly Gillen provided constant help through all the paperwork and logistics arrangement, and gave professional edits in the preparing of my publications. I feel fortunate to work with other talented members in the lab, Kofi Deh, Sarah Eskreis-Winkler, Yan Wen, Junghun Cho, Ramin Jafari, Jinwei Zhang, Qihao Zhang, Liangdong Zhou, who have provided with a mixture of insight and encouragement.

Finally, I would like to acknowledge the members on my special committee, Dr. Yi Wang, Dr. Peter Doerschuk and Dr. Martin Prince, for agreeing to examine this thesis.

TABLE OF CONTENTS

LIST OF FIGURES

LIST OF TABLES

No table of figures entries found.

LIST OF ABBREVIATIONS

CG	Conjugate Gradient
CMB	Cerebral Micro Bleed
CNN	Convolutional Neural Network
COSMOS	Calculation Of Susceptibility through Multiple Orientation Sampling
CSF	Cerebrospinal Fluid
DL	Deep Learning
FA	Flip Angle
FOV	Field Of View
ICH	Intracerebral Hemorrhage
MEDI	Morphology Enabled Dipole Inversion
MRI	Magnetic Resonance Imaging
MS	Multiple Sclerosis
NAWM	Normal Appearing White Matter
PDF	Projection onto Dipole Fields
QSM	Quantitative Susceptibility Mapping
RMSE	Root Mean Square Error
ROI	Region Of Interest
SNR	Signal Noise Ratio
TE	Echo Time
TFI	Total Field Inversion
TR	Repetition Time

CHAPTER 1

1 INTRODUCTION

Magnetic susceptibility is an intrinsic physical property of material that is useful for the identification and quantification of biomarkers such as iron, calcium and gadolinium. It can directly reflect the concentration of paramagnetic or diamagnetic materials, making a consistent and robust implementation of quantitative susceptibility measurement much desirable in various applications. Quantitative Susceptibility Mapping (QSM) has advanced MRI study of tissue magnetism in characterizing the pathology of various diseases (1). For instance, the susceptibility value of Multiple Sclerosis lesions (2-5) could be measured and compared to normal white matter. This measurement, as a synergy of iron accumulation and demyelination, could be used to characterize the progressive stage of MS. Other applications involve Alzheimer's disease (6), Parkinson's disease (6-8), Huntington's disease (6, 8), intracerebral hemorrhage (9), stroke (10) and calcification (11).

However, MRI cannot directly measure the tissue magnetic susceptibility. In order to estimate the susceptibility distribution from MRI signal, we need to review the physical model through which susceptibilities affect the phase component of the MRI signal. We will then introduce the basic procedure of solving the inverse problem from MRI signal to susceptibility recovery. Finally, we specify the limitations of the conventional QSM procedure and propose novel algorithms to address these limitations as major contribution of the current thesis.

1.1 Magnetic Susceptibility, Field and Phase

In this section, we examine the forward process by which a magnetic susceptibility distribution generates an inhomogeneous magnetic field and in turn modulates the phase signal in the MRI image.

When tissue material is placed in an external magnetic field, such as the main magnetic field of an MRI scanner, the relation between its magnetization $\mathbf{M}$ (magnetic moment per unit volume) and the external magnetic field $\mathbf{H}$ is defined as:

$$\chi = \frac{\mathbf{M}}{\mathbf{H}} \qquad [1.1]$$

where χ is the magnetic susceptibility. It indicates the magnitude of tissue magnetic perturbation in an external applied field, an intrinsic property of material that categorizes them into paramagnetic ($\chi > 0$) or diamagnetic ($\chi < 0$) material. For instance, iron, as a critical metal element in many bio-physiological functions, is paramagnetic, while calcium as associated with mineralization and calcification processes, is diamagnetic.

A distribution of spatially varying susceptibility sources will perturb the external applied magnetic field. We can derive the exact relation by which tissue susceptibility determines the field perturbation using the Maxwell's equations (12-14) and Lorentz sphere correction model (15, 16), resulting in the following convolutional form for non-ferromagnetic tissue ($\chi \ll 1$) (See Appendix A for the detailed derivation):

$$\frac{b}{B} = d * \chi \qquad [1.2]$$

where B is the external magnetic field strength, b is the observed perturbation field by the tissue and d is the dipole kernel used in the convolution operation $*$, which can be regarded as the magnetic field perturbed by a unit point susceptibility source:

$$d(\boldsymbol{r}) = \frac{1}{4\pi}\frac{3\cos^2\theta - 1}{|\boldsymbol{r}|^3}, \qquad \boldsymbol{r} \neq \mathbf{0} \tag{1.3}$$

θ is the angle between the location vector $\boldsymbol{r}$ and the main magnetic field $\boldsymbol{B}$. The dipole kernel (Eq. 1.3) has a Fourier transform:

$$D(\boldsymbol{k}) = \mathcal{F}\{d\} = \frac{1}{3} - \frac{k_z^2}{k^2}, \qquad \boldsymbol{k} \neq \mathbf{0} \tag{1.4}$$

which leads to the following Fourier multiplication form of Eq. 1.2:

$$\mathcal{F}\left\{\frac{b}{B}\right\} = D \cdot \mathcal{F}\{\chi\} \tag{1.5}$$

If the MRI images are acquired using gradient echo sequence, the complex MRI signal, after de-modulation of the spatial encoding gradient field, reflects the perturbed magnetic field in a linear fashion via its phase component:

$$I = me^{-R2^*\mathrm{TE}}e^{-\mathrm{i}2\pi b\mathrm{TE}} + n \tag{1.6}$$

where m is the magnitude of the magnetization damped with an exponential R2* decay, TE is the acquisition time for the corresponding gradient echo and n is random noise. Note that the phase component is proportional to the perturbation field b with a factor of $2\pi\mathrm{TE}$.

1.2 Quantitative Susceptibility Mapping

QSM essentially solves the inverse problem that decodes the susceptibility map χ through processes Eq. 1.2 and Eq.1.6. Considering the presence of noise and an exponential decay of the signal magnitude in Eq. 1.6, a least square fitting can be performed on the phases at multiple TEs to obtain the raw estimate the strength of the perturbation field (17):

$$b_{\mathrm{raw}} = \arg\min_{b} \sum_{j=1}^{N_{\mathrm{TE}}} \left\| I_j - \left| I_j \right| e^{\mathrm{i}2\pi b \mathrm{TE_j}} \right\|_2^2 \qquad [1.7]$$

This least square fitting could also provide an estimate of the noise level (17, 18) in the field map b_{raw}, and use its inverse as an SNR weighting w. Eq. 1.7 is typically followed by a phase unwrapping algorithm (18, 19) to remove the intrinsic 2π phase wraps between adjacent voxels, giving a continuous field estimation b.

Given the field estimation, the inverse problem of solving for the underlying susceptibility map remains nontrivial. It presents two intrinsic challenges (1, 20) that preclude a straightforward calculation of the susceptibility map.

First, the estimated magnetic field contains two components: background field and local field. The background field is defined as the field contribution of sources outside the region of interest (ROI), where a reliable measurement of phase signal is absent due to low or negligible MR signal. Examples include air surrounding the head and inside the sinus system, and the cortical bone in the skull and neck. Background field contribution might also include macroscopic field modulation such as B0 field

imperfection or the shimming field from the MR scanner. On the other hand, the local field is defined as the field generated by the tissue inside the ROI, such as the gray/white matter, veins or CSF. The correct separation of background field and local field is essential to the accurate depiction of the brain tissue susceptibility map, which has been shown to be challenging: the background field is usually by orders of magnitude stronger than the local field, such that it requires dedicated approaches (21-23) to efficiently extract and remove this background field in the presence of a much weaker local field. More details on those approaches will be discussed in Chapter 4: Preconditioned Total Field Inversion.

Second, upon a successful estimation of the local tissue field, we need to solve an inverse problem for the tissue susceptibility distribution. This is an ill-posed inverse problem, due to the singularity of the dipole kernel in the Fourier domain (Eq. 1.4). Specifically, the dipole kernel D is zero on a pair of opposing cone surfaces at the magic angle $\theta \sim 54.7°$ (or equivalently, $\frac{k_z^2}{k^2} = \frac{1}{3}$) with respect to the main magnetic field direction (Figure 1.1).

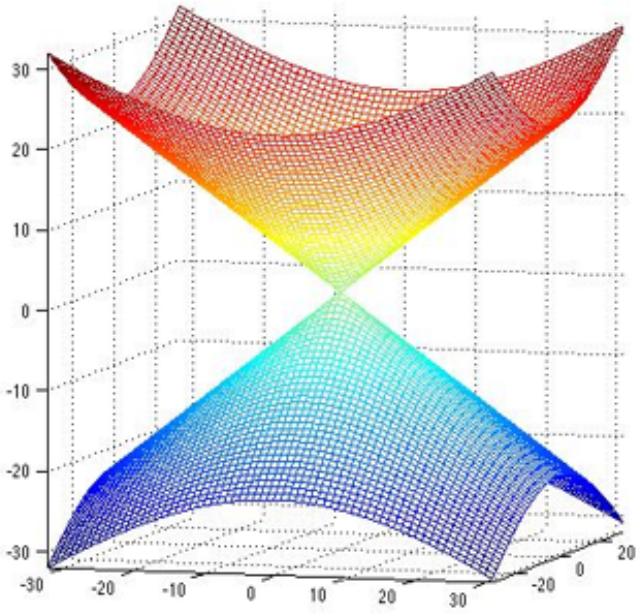

Figure 1.1. The double cone surfaces for the dipole kernel in k-space.

Failure to handle this singularity causes streaking artifact along the magic angle in the susceptibility map, hence degrading its diagnostic value. Researchers have proposed numerous approaches (24-27) that incorporate regularization in either k-space or image space to tackle this streaking artifact. Conventional regularizations such as total variation (20, 27) promote specific assumptions on the smoothness or sparsity of the image by itself, or in a transformed domain like gradient or wavelet domain. One of the most popular approaches is Morphology Enabled Dipole Inversion (MEDI) (18, 26, 27):

$$\chi^* = \underset{\chi}{\operatorname{argmin}} \frac{1}{2} \left\| w\left(e^{-if} - e^{-i(d*\chi)}\right) \right\|_2^2 + \lambda_1 \| M_G \nabla \chi \|_1 \qquad [1.8]$$

which employs a total variation regularization weighted with an edge mask M_G to maintain structural consistency with the magnitude MR image. Here $f = b/B_0$ is the normalized local field. However, such built-in assumption might overlook the fine structure in the susceptibility map that has high spatial frequencies. Therefore, in Chapter 3 we design a machine learning based regularization to exploit the capacity of deep learning, in order to achieve better structural recovery.

Even with proper regularization, the streaking artifact might intensify with the presence of strong susceptibility sources (e.g. hemorrhage) and over-shadow the surrounding normal gray/white matter (28-30). Chapter 4 presents a novel concept called preconditioning that suppresses shadowing artifact in both normal and hemorrhage scenarios (9, 29).

In interpretation of the susceptibility measurements, one should note the presence of an arbitrary constant component across the entire QSM which is indifference on the perturbation field. The reason is that: the dipole kernel is 0 at the origin of k-space ($\boldsymbol{k} = \mathbf{0}$) in its implementation (Eq. 1.4), thereby discarding any DC component from the susceptibility map χ. In other words, a referencing scheme becomes essential in cross-subject and cross-center susceptibility study. Chapter 2 provides an automated procedure to determine this QSM reference.

1.3 Summary of Contribution

The work in this thesis is designed to develop robust numerical algorithms to reliably perform quantitative susceptibility mapping under various scenarios. Three new

technical developments are proposed, each described in a separate chapter.

1. **CSF regularization in QSM for automated zero reference**. Chapter 2 presents an augmented QSM reconstruction model that employs a dedicated regularization design to enforce the homogeneity of CSF susceptibility in its solution (31). This approach removed the manual effort in choosing the CSF reference ROI, reduced the uncertainty of zero reference caused by the CSF flow or white matter anisotropy, and improved the image quality in the white matter adjacent to the ventricular CSF. Numerical analysis on MS patient suggested that this regularized approach maintained well agreement with a conventional approach in quantifying lesion-white matter contrast,.

2. **Deep learning based regularization for QSM**. Chapter 3 proposes to incorporate a convolutional neural network (CNN) model into the traditional numerical optimization framework for QSM reconstruction. Unlike the direct feedforward computation through the network, a feedback scheme was used to enforce the consistency of the reconstructed susceptibility map with the actual field measurement through a fidelity cost; Meanwhile, the outcome of the CNN was incorporated via a regularization term, which penalized the deviation between the solution and the CNN reference map. It outperformed a traditional total variation regularized model at less computational costs.

3. **Preconditioned Total Field Inversion**. Chapter 4 presents a novel framework that bypasses the separate fittings for background field and local field components. Instead, it fit for a susceptibility distribution over the entire field of view from the total field

estimation. This generalized framework, named Total Field Inversion (30), eliminated error propagation and improved the accuracy of the susceptibility recovery, especially for susceptibility source close to ROI boundaries. It also preserved the image quality in the presence of severe susceptibility contrasts, such as those in intracerebral hemorrhage (ICH) patient.

CHAPTER 2

2 CSF REGULARIZATION IN QSM FOR AUTOMATED ZERO REFERENCE

2.1 Abstract

In this chapter we developed a quantitative susceptibility mapping (QSM) method with an automated zero reference using minimal variation in cerebrospinal fluid (CSF) susceptibility.

2.2 Introduction

QSM provides meaningful susceptibility measurement only with respect to a chosen reference tissue. This comes from the fact that an arbitrary constant shift in QSM produces no difference in the perturbation field because of the singularity of dipole kernel at the k-space center (Eq. 1.4). Accordingly, a common tissue is determined whose susceptibility is subtracted from the entire QSM. This tissue is referred to as zero reference tissue. It is necessary for cross-subject and cross-institute studies. For brain QSM, cerebrospinal fluid (CSF) is a popular zero reference choice due to its chemical resemblance to pure water (32). However, ventricular CSF in traditional QSM is often inhomogeneous, and causes uncertainty of the reference susceptibility (32, 33). Literature suggests that CSF flow (10, 34) and white matter anisotropy (35) might be the reason to this variation in susceptibility.

Considering that regularization has been used to address streaking artifacts in QSM

which are caused by amplified noise during the ill-posed field-to-source inversion (36, 37) such as in current Bayesian QSM (morphology enabled dipole inversion, MEDI (18, 38), we could similarly use regularization to suppress ventricular CSF susceptibility inhomogeneity. In fact, applying scalar version of field-to-source inversion on field which contains contribution from anisotropic white matter, may have non-local influence to QSM, particularly around ventricles that are adjacent to white matter tracts. We design a regularization that specifically enforces the susceptibility uniformity inside the ventricular CSF. In this chapter, we show preliminary data demonstrating that minimal susceptibility variation in CSF can be achieved for a consistent and automated zero reference of QSM, and further provide improvement on image quality. This method is referred to as MEDI+0 (31).

2.3 Theory

The optimization problem for QSM in literature has become a MEDI type Bayesian framework (1, 39-43):

$$\chi^* = \underset{\chi}{\operatorname{argmin}} \frac{1}{2} \left\| w\left(e^{-if} - e^{-i(d*\chi)}\right) \right\|_2^2 + \lambda_1 \| M_G \nabla \chi \|_1 \qquad [2.1]$$

with χ the susceptibility map, $*$ the convolution operation, w the noise weighting, f the measured local field, ∇ the gradient operator and M_G the binary edge mask derived from the magnitude image (18). d is the dipole kernel which can be defined in both Fourier and spatial domains:

$$d = \frac{1}{4\pi} \frac{3\cos^2(\theta) - 1}{r^3} = \mathrm{FT}\left[\frac{1}{3} - \frac{k_z^2}{k^2}\right] \qquad [2.2]$$

In this work, we propose a method named MEDI+0 (31) which solves:

$$\chi^* = \underset{\chi}{\operatorname{argmin}} \frac{1}{2} \left\| w\left(e^{-if} - e^{-i(d*\chi)}\right) \right\|_2^2 + \lambda_1 \|M_G \nabla \chi\|_1 + \lambda_2 \|M_{CSF}(\chi - \overline{\chi_{CSF}})\|_2^2, \quad [2.3]$$

which adds to MEDI (Eq. 2.1) an L_2-regularization where M_{CSF} denotes the ROI of ventricular CSF and $\overline{\chi_{CSF}}$ mean susceptibility within M_{CSF}. This additional term penalizes susceptibility variation within M_{CSF} to obtain a solution with homogeneous CSF susceptibility.

An automated procedure is designed here to determine the ventricular CSF mask M_{CSF} from the brain ROI mask M and the R_2^* map, considering the fact that CSF typically has low R_2^*. It consists of the following stages:

(a) Threshold R_2^*: $M_{R_2^*} \triangleq R_2^* < R$, for a given threshold R.

(b) Define brain centroid: $\boldsymbol{c} = \frac{1}{N} \sum_{\boldsymbol{r} \subset M} \boldsymbol{r}$, where N is the number of voxels in M.

(c) Define central brain region: $M_c \triangleq \{\boldsymbol{r} | \|\boldsymbol{r} - \boldsymbol{c}\|_2 < 3\text{cm}\}$.

(d) Analyze connectivity in $M_c \cap M_{R_2^*}$: divide $M_c \cap M_{R_2^*}$ into connected components M_{ci} (6-neighbour) and merge the largest 3 components: $M_{cCSF} \triangleq \{M_{c1} \cup M_{c2} \cup M_{c3}\}$.

(e) Analyze connectivity in $M_{R_2^*}$: divide $M_{R_2^*}$ into connected components M_i (6-neighbour) and merge all components that overlap with M_{cCSF}: $M_{CSF} \triangleq \{\bigcup M_i \,|M_i \cap M_{cCSF} \neq \emptyset\}$.

The proposed approach contains two new parameters: (λ_2, R), which will be chosen in the numerical simulation. The problem in Eq. 2.3 is solved using Gauss Newton Conjugate Gradient (18). As a final step, $\overline{\chi_{CSF}}$ is subtracted from the entire map for zero reference.

2.4 Methods and Materials

2.4.1 Numerical Simulation

We constructed a numerical brain phantom to simulate the CSF inhomogeneity related to anisotropic susceptibilities from white matter (Figure 2.1). The susceptibility tensor was originally reconstructed from a 12-orientation acquisition (matrix size=256×256×126, voxel size=1×1×1.5 mm, ΔTE=2.6 ms) in (44) using susceptibility tensor imaging (STI) (45). The ventricular CSF region was manually drawn by an experienced radiologist. Under the assumption that ventricular CSF is homogeneous and not a source of susceptibility anisotropy, susceptibility was chosen to be 0 within CSF. Then the field was generated in two ways: first, a tissue field f_{aniso} was generated with $\{\chi_{13}, \chi_{23}, \chi_{33}\}$ using the anisotropic forward model:

$$f_{\text{aniso}} = \text{FT}^{-1}\left[\left(\frac{1}{3} - \frac{k_z^2}{k^2}\right)\text{FT}[\chi_{33}] - \frac{k_x k_z}{k^2}\text{FT}[\chi_{13}] - \frac{k_y k_z}{k^2}\text{FT}[\chi_{23}]\right] \quad [2.4]$$

Second, a tissue field f_{iso} was generated merely with χ_{33} using the isotropic forward model:

$$f_{\text{iso}} = \text{FT}^{-1}\left[\left(\frac{1}{3} - \frac{k_z^2}{k^2}\right)\text{FT}[\chi_{33}]\right] \quad [2.5]$$

MEDI and MEDI+0 were applied to both fields. The root-mean-square-error (RMSE) between the reconstructed χ and the true susceptibility map χ_{33}, $\|\chi - \chi_{33}\|_2 / \|\chi_{33}\|_2$, was calculated. λ_1 was determined by minimizing RMSE for MEDI (Eq. 2.1), and the same value was used for MEDI+0 (Eq. 2.3). λ_2 and R in MEDI+0 were jointly determined through minimizing RMSE. RMSE within the region in 10mm proximity to the ventricular CSF was also calculated.

2.4.2 In Vivo Experiment: Multiple Sclerosis

The brains of 8 patients with Multiple Sclerosis (MS) were scanned at 3T (GE, Milwaukee, WI). All studies in this work were approved by our Institutional Review Board. Imaging sequences were: 3D T2*w spoiled multi-echo GRE (Flip angle=20, FOV=24 cm, TE1=4.3 ms, TR=57 ms, #TE=11, ΔTE=4.8 ms, acquisition matrix=512×512×68, voxel size=0.47×0.47×2 mm^3, BW=±62.5 kHz, A/P monopolar readout with flow compensation for all echoes, parallel imaging factor R=2 and a total scan time of ~10 min) and T2w fast spin echo (Flip angle=90, FOV=24 cm, TE=86 ms, TR=5250 ms, slice thickness=3 mm, acquisition matrix=416×256×68). Nonlinear field map estimation and graph-cut-based phase unwrapping (19) were applied to obtain a total field estimation, then projection onto dipole fields (PDF) (21) was used

for background field removal in order to obtain the local field. Next, using the same input local field, MEDI+0 was compared with MEDI, which had been previously used for MS lesion assessment (2, 46). An experienced radiologist drew an ROI of each lesion on the T2w images, which were co-registered onto magnitude images of the T2*w scan. Reference regions for lesion susceptibility were determined by drawing an ROI in the normal appearing white matter (NAWM) on the contralateral side of the identified lesion (46). The difference of mean susceptibilities between the lesion and NAWM was measured and analyzed with linear regression and Bland-Altman analysis to quantify the agreement between MEDI and MEDI+0.

2.5 Results

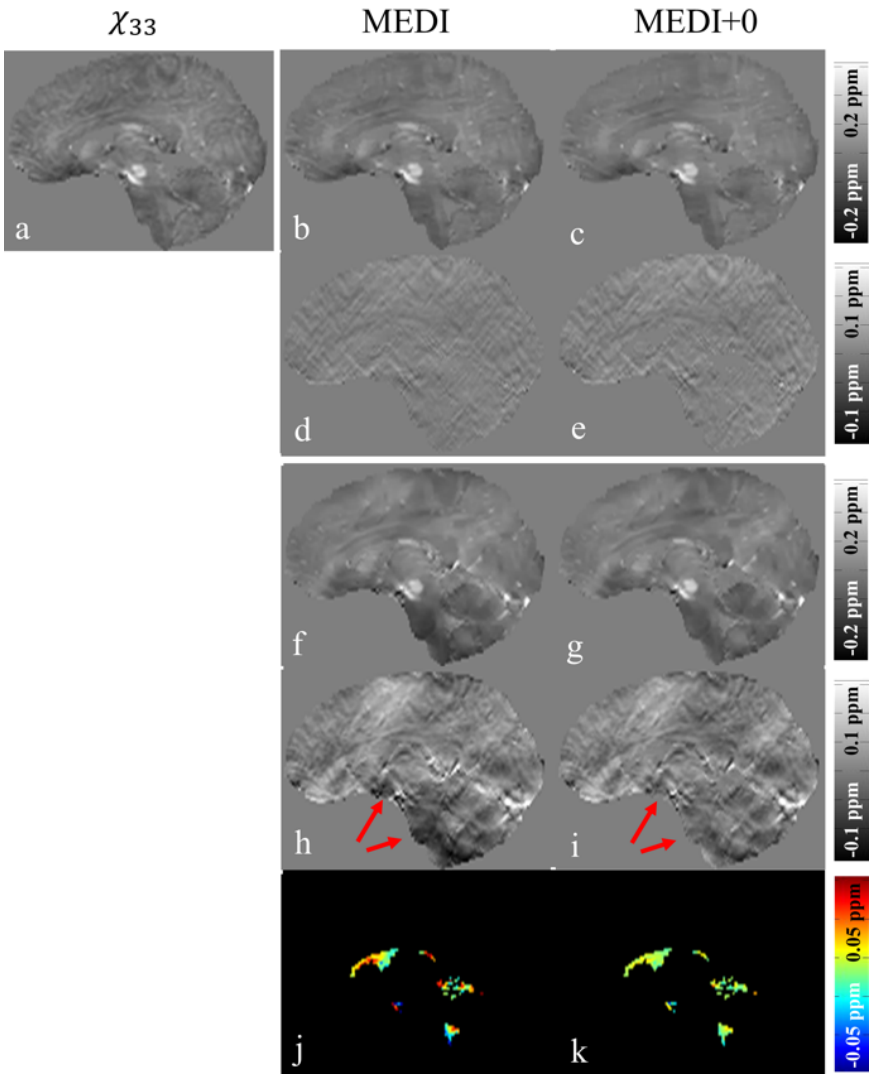

Figure 2.1. Simulation result.

(a) $\boldsymbol{\chi_{33}}$*. When* $\boldsymbol{f_{iso}}$ *is used as input field, QSM is shown for MEDI (b) and MEDI+0 (c). When* $\boldsymbol{f_{aniso}}$ *is used as input field, QSM is shown for MEDI (f) and MEDI+0 (g). (d, e, h, i) are the difference maps between (b, c, f, g) and* $\boldsymbol{\chi_{33}}$ *(a), respectively. The CSF susceptibility in (f, g) is highlighted in (j, k) respectively.*

2.5.1 Numerical Simulation

Figure 2.1 shows the comparison of true susceptibility χ_{33}, QSM reconstructed with MEDI and MEDI+0 given field input f_{aniso} and f_{iso}, respectively. Given f_{iso} as the input, both MEDI and MEDI+0 achieved relatively small RMSEs (22.4% and 29.1% respectively) with respect to χ_{33}. The standard deviation of susceptibility within the segmented ventricular region was 5.1ppb for MEDI and 1.7ppb for MEDI+0. While susceptibility anisotropy was simulated (f_{aniso}), MEDI+0 produced a lower RMSE (73.7%) than MEDI (76.1%). The RMSE within a 10mm proximity of the ventricular CSF mask was 65.1% for MEDI+0 and 73.5% for MEDI, reflecting a reduced negative shadow artifact in the white matter (red arrows in Figs. 2.1h and 2.1i). The standard deviation of susceptibility within the ventricular CSF were 28.1ppb for MEDI and 9ppb for MEDI+0. This reduced variation for MEDI+0 was also reflected in the highlighted CSF QSM in Figs. 2.1j and 2.1k.

The optimized parameters values were $\lambda_1 = 0.001$ for MEDI and $\lambda_1 = 0.001, \lambda_2 = 0.1, R = 5\ \text{s}^{-1}$ for MEDI+0. These values were used throughout this work.

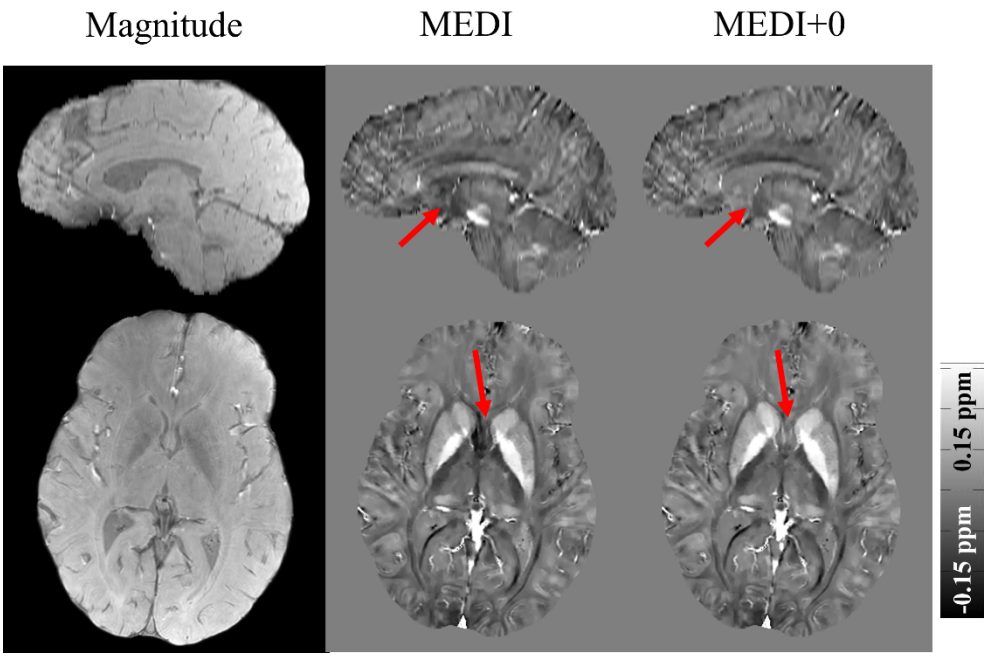

Figure 2.2. In vivo QSM reconstruction.

Examples of magnitude (left), QSM using MEDI (middle) and MEDI+0 (right). A hypo-intensity artifact close to anterior horn of the lateral ventricles is suppressed using MEDI+0 (indicated by red arrows).

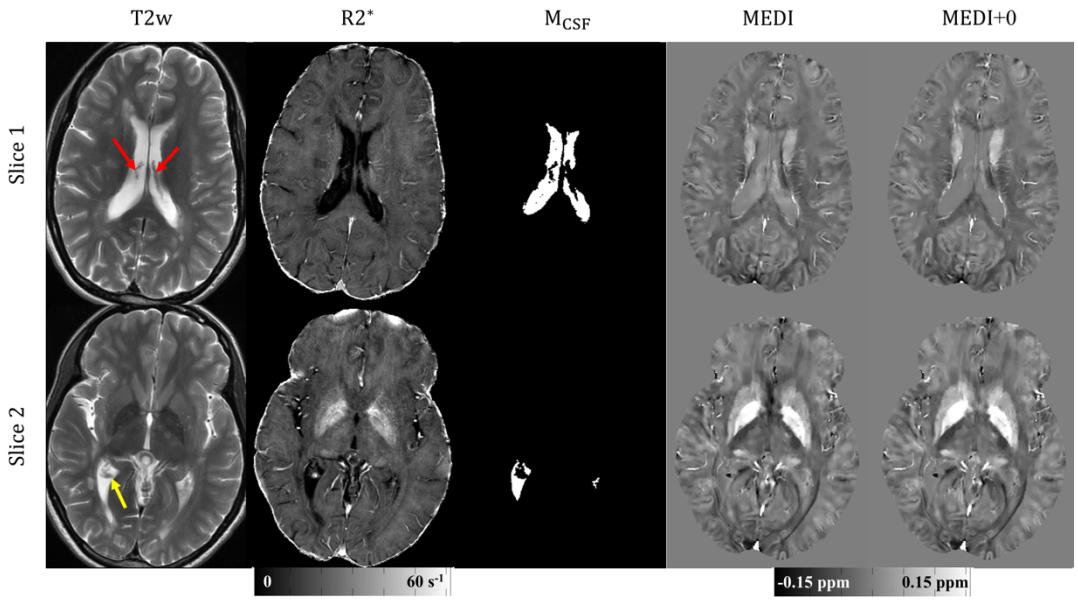

Figure 2.3. In vivo CSF segmentation.

From left to right: T2w images, R2 map, segmented CSF ROI, QSM reconstructed by MEDI and MEDI+0. Choroid plexus is observed with low signal on T2w image (indicated by arrows) and high R2*. The proposed segmentation procedure excludes the choroid plexus by its high R2*. MEDI+0 improves the homogeneity of the CSF only, while preserving the paramagnetic vascular structure of choroid plexus (red arrows) and the diamagnetic calcification (yellow arrow).*

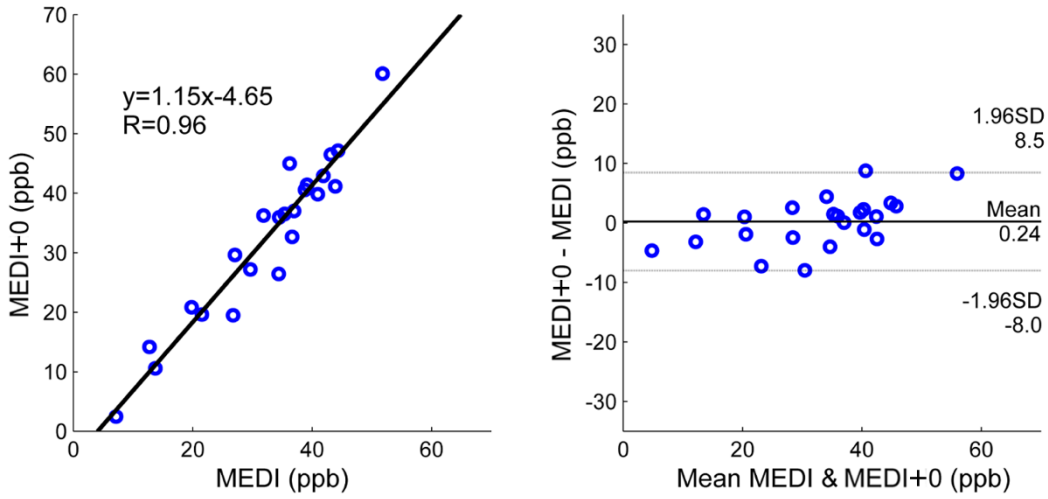

Figure 2.4. Scatter and Bland-Altman analysis of MS lesion measurement. Scatter (left) and Bland-Altman (right) plots of QSM measurements of all 23 Multiple Sclerosis lesions relative to NAWM. This demonstrates strong correlation (k=1.15, R=0.96), a small bias of 0.24ppb and 95% limits of agreement of [-8.0, 8.5] ppb.

2.5.2 In Vivo Experiment: Multiple Sclerosis

Figure 2.2 shows an example of reconstructed brain QSMs using MEDI and MEDI+0 for one MS patient. Hypo-intense shadow artifacts were reduced in the region under the horns of lateral ventricle and anterior to the substantia nigra, indicated by red arrows in Figure 2.2. The standard deviation of susceptibility within M_{CSF} was 5-fold lower in MEDI+0 as compared to MEDI.

Figure 2.3 shows the T2w image, R_2^* map, segmented CSF mask, MEDI and MEDI+0 results in two axial cross sections of one MS patient data. It was observed

that structures within the ventricles were heterogeneous, particularly in the choroid plexus which was hypo-intense T2w image and hyper-intense on R_2^*. The proposed segmentation procedure detected CSF while excluding the choroid plexus with $R_2^* > R = 5s^{-1}$, thereby only improved the homogeneity of ventricular CSF and preserved paramagnetic vascular structure (red arrows) and diamagnetic calcification (yellow arrows) in the choroid plexus.

In measurements of lesion susceptibility relative to NAWM, MEDI+0 showed a strong correlation with MEDI ($k = 1.15,\ R = 0.96$) for all 23 lesions from 8 patients (Figure 2.4). Bland-Altman analysis of MEDI+0 compared to MEDI suggested a small bias of 0.24ppb with narrow [-8.0, 8.5] ppb 95% limits of agreement.

2.6 Discussion

In this chapter, the MEDI+0 method is proposed using automated ventricle segmentation procedure combined with an L_2-regularization on ventricular CSF susceptibility variation. Our data demonstrate that MEDI+0 reduces anisotropy related artifacts. Furthermore, MEDI+0 does not alter the tissue contrast between MS lesions and NAWM.

Zero referencing is essential to QSM, because the measured tissue field is invariant with any constant shift in the susceptibility source. CSF is a common choice as zero reference tissue, while it is typically extracted using a manually drawn ROI in the posterior of the lateral ventricles (32). However, the size of the ventricles strongly varies across subjects (32), and CSF often appears non-uniform in QSM, rendering the

measured CSF value much sensitive to the choice of this segmented ROI (33). This induces an cross-subject uncertainty in the zero reference. The MEDI+0 method utilizes a known uniformity (47) to address this zero reference issue in two aspects; First, it removes the manual segmentation of the CSF ROI, while the ventricular CSF is automatically segmented and provided as zero reference region. Second, it enforces CSF homogeneity during numerical optimization and reduces the sensitivity of zero reference to the ROI.

The insight for the described CSF-specific regularization comes from studying the origin of the CSF inhomogeneity in current QSM, which may be mainly induced by anisotropy of the surrounding white matter tracts (35). The anisotropic influence of white matter on the frequency map has been extensively studied in literature (44, 45, 48-59). It is suggested that scalar dipole inversion cannot fully resolve the non-local influence of white matter anisotropy. The unresolved component might induce non-local artifacts expanding towards nearby regions. In the current work, white matter tracts were present adjacent to the ventricles. This effect was investigated using a numerical phantom, where the field contribution of anisotropic components (χ_{13} and χ_{23}), demonstrated as $f_{\text{aniso}} - f_{\text{iso}}$, generated spatially smooth shadow artifacts in QSM in Figs. 2.1h and 2.1i. With the CSF homogeneity enforced in MEDI+0, shadow artifacts were markedly reduced at the deep brain nuclei in simulation (Figure 2.1i) and in vivo (Figure 2.2). The L_2-regularization in MEDI+0 demonstrated a non-local artifact suppression in both the interior and neighborhood of CSF.

The L_2-regularization of CSF susceptibility conceptually employed a Bayesian strategy

for streaking reduction. The CSF susceptibility inhomogeneity and related shadow artifacts may be considered as effects from spatially smooth errors, such as $f_{\text{aniso}} - f_{\text{iso}}$. A corresponding strategy to reduce these artifacts is to employ a prior term that promotes CSF homogeneity, as described in MEDI+0. It is noted that de Rochefort (47) proposed a similar framework penalizing the L_2-norm of χ itself rather than $\chi - \bar{\chi}$ as used in the current work.

MEDI+0 may directly improve the depiction of deep gray nuclei, including the subthalamic nucleus, which is an important surgical target of deep brain stimulation (60). The zero reference in MEDI+0 might benefit longitudinal studies as in temporal investigation of multiple sclerosis lesion development (2), for estimating the oxygenation level of venous blood (7, 34, 61) and tissue (10), and for differentiating diamagnetic materials from paramagnetic ones (3, 11). Specifically, for measuring susceptibility difference between MS lesions and NAWM (Figure 2.4), the strong agreement between MEDI and MEDI+0 suggests that MEDI+0 does not introduce significant changes in this relative tissue contrast. Therefore, MEDI+0 can be readily applied to the lesion analysis as in literature (2, 3, 46).

2.7 Conclusion

In summary, the proposed MEDI+0 method uses automated segmentation of CSF and enforcement of susceptibility homogeneity within the ventricular CSF to reduce QSM artifacts from susceptibility anisotropy and provides a consistent zero reference for QSM.

CHAPTER 3

3 QUANTITATIVE SUSCEPTIBILITY MAPPING USING A DEEP LEARNING PRIOR

3.1 Abstract

To propose a Quantitative Susceptibility Mapping (QSM) reconstruction using deep learning (DL) based regularization in the Bayesian approach. A 3D convolutional neural network (CNN) was trained to map the tissue field to susceptibility using healthy subject data. The CNN outcome of susceptibility was then used in a traditional regularized QSM reconstruction constraining the L_2 discrepancy between the solution and the network outcome. The proposed method, named MEDI+DL, aimed to improve anatomical detail while maintaining accuracy of susceptibility quantification compared with a traditional regularized method, Morphology Enabled Dipole Inversion (MEDI), in healthy subjects and multiple sclerosis (MS) patients.

3.2 Introduction

QSM reconstruction is a Bayesian optimization problem obtaining a susceptibility distribution that is consistent with the tissue inhomogeneity field measurement through dipole convolution. Because of the ill-posed condition of the dipole convolution inverse problem, a structural prior is used to suppress streaking and other artifacts (20). However, explicit regularization is limited in defining image features with prior knowledge; for example, fine structures such as veins may be less well visualized in the typically smooth or blocky solutions using common L_2 or L_1

regularizations, respectively.

Recently, convolutional neural networks (CNN) in deep learning have been proposed for QSM reconstruction (62, 63), as they are advantageous in characterizing image features. A CNN directly maps the local field to the susceptibility map, hence bypassing the traditional iterative optimization and reducing the computational cost down to a single forward evaluation of the network. The network can be trained on labeled datasets such as numerical phantoms (62), or images from healthy subjects reconstructed using COSMOS (63), thus demonstrating the feasibility of a deep learning (DL) solution for QSM. However, this approach fails to enforce the fidelity between a measured field and its corresponding DL susceptibility output; this failure may be substantial when applied on populations that are different from those used in training.

In this work, we impose an explicit data fidelity in DL based QSM reconstruction such that the output of the CNN trained to map from field to QSM is incorporated as a Bayesian prior (64, 65) in the QSM optimization problem. We report preliminary results showing QSM improvements by this combined fidelity and DL approach.

3.3 Theory

The fundamental inverse problem in QSM reconstruction is to obtain a susceptibility distribution χ from the measured tissue field f. Given a sample dataset where susceptibility is known, a neural network $\phi(\cdot)$ can be trained to simulate the inversion process, i.e., to learn the mapping from field to susceptibility (62, 63):

$$\chi_\phi = \phi(f) \qquad [3.1]$$

However, this network does not explicitly consider the fidelity when mapping a newly measured field f to the corresponding network output. In this work, we employ a Bayesian reconstruction framework (64, 65) that incorporates the neural network outcome into an optimization problem:

$$\chi^* = \underset{\chi}{\operatorname{argmin}} \frac{1}{2} \left\| w\left(e^{-if} - e^{-i(d*\chi)}\right) \right\|_2^2 + \lambda_2 \left\| E\left(\chi - \chi_\phi\right) \right\|_2^2 \qquad [3.2]$$

The first term is the data fidelity penalty as in the traditional QSM reconstruction, with w the noise weighting and d the dipole kernel. The second term is an L_2-regularization that penalizes the discrepancy between χ and the estimated map χ_ϕ given by the network ϕ. Here, E is a linear transformation, which can be the identity or a filter that enhances specific properties of the solution. The design of E will be explained in the Methods section.

The Bayesian rational for this L_2-regularization is a prior that $E\chi$ belongs to an independent and identically distributed (i.i.d.) Gaussian distribution $\mathcal{N}\left(E\chi_\phi, \lambda_2^{-1}\right)$ at each voxel (64). A similar Bayesian framework can be found in Morphology Enabled Dipole Inversion (MEDI):

$$\chi^* = \underset{\chi}{\operatorname{argmin}} \frac{1}{2} \left\| w\left(e^{-if} - e^{-i(d*\chi)}\right) \right\|_2^2 + \lambda_1 \| M_G \nabla \chi \|_1 \qquad [3.3]$$

where an L_1-norm of the image gradients weighted by a binary edge mask M_G is used for regularization. This consists of a prior that $M_G \nabla \chi$ should be sparse. Considering

the necessity of zero-referencing for susceptibility quantification, an extra L_2 regularization can enforce a uniform ventricular cerebrospinal fluid (CSF) signal, as is used in MEDI+0 (31):

$$\chi^* = \underset{\chi}{\operatorname{argmin}} \frac{1}{2} \left\| w\left(e^{-if} - e^{-i(d*\chi)}\right) \right\|_2^2 + \lambda_1 \|M_G \nabla \chi\|_1 + \lambda_{\mathrm{CSF}} \|M_{\mathrm{CSF}}(\chi - \overline{\chi_{\mathrm{CSF}}})\|_2^2 \quad [3.4]$$

where M_{CSF} is a binary mask for ventricular CSF and $\overline{\chi_{\mathrm{CSF}}}$ is the mean susceptibility within it. Similarly, this CSF-specific regularization can be added to Eq. 3.2, leading to the final proposed objective:

$$\chi^* = \underset{\chi}{\operatorname{argmin}} \frac{1}{2} \left\| w\left(e^{-if} - e^{-i(d*\chi)}\right) \right\|_2^2 + \lambda_2 \left\| E\left(\chi - \chi_\phi\right) \right\|_2^2 + \lambda_{\mathrm{CSF}} \|M_{\mathrm{CSF}}(\chi - \overline{\chi_{\mathrm{CSF}}})\|_2^2 \quad [3.5]$$

In this work, the proposed method (Eq. 3.5) is referred to as MEDI+DL. It will be compared with χ_ϕ, the raw outcome of the deep learning network which is referred to as DL, and with MEDI+0 (Eq. 3.4), which is referred to as MEDI throughout this work for brevity.

3.4 Methods and Materials

3.4.1 Data Acquisition and Processing

All data were acquired using a 3D multi-echo GRE sequence on a 3T GE scanner (voxel size $0.5 \times 0.5 \times 3\mathrm{mm}^3$, field of view 24cm, ΔTE 4.8ms, number of echoes 8, TR 49ms, number of slices 50~60, bandwidth $\pm$62.5 kHz) with matrix size

$512 \times 512 \times 50{\sim}60$. 20 healthy subjects and 8 patients with Multiple Sclerosis (MS) were scanned, according to approved Institutional Review Board protocols. All subjects gave written informed consent. The local tissue field was estimated through multi-echo phase fitting (17), phase unwrapping (19) and background field removal (21). 4 of the 20 healthy subjects were scanned using the same sequence at a voxel size of $1\times 1 \times 1\text{mm}^3$ with 5 different orientations to perform COSMOS reconstruction (66) for quantitative comparison.

3.4.2 Neural Network Setup

U-Net (62, 63, 67), a fully convolutional neural network, was chosen as the network structure. We used a $3 \times 3 \times 3$ kernel, 1 voxel stride, and reflective padding at each convolution layer. The detailed structure regarding layer numbers, up/down-sampling factors, and feature dimensions can be found in Figure 3.1. The network was designed for an input/output patch of size $128 \times 128 \times 24$, while the original 3D volume field map was segmented into overlapping patches: each patch had a 66% overlap with each of its neighbors in each spatial direction. The output patches were compiled to recover the full volume.

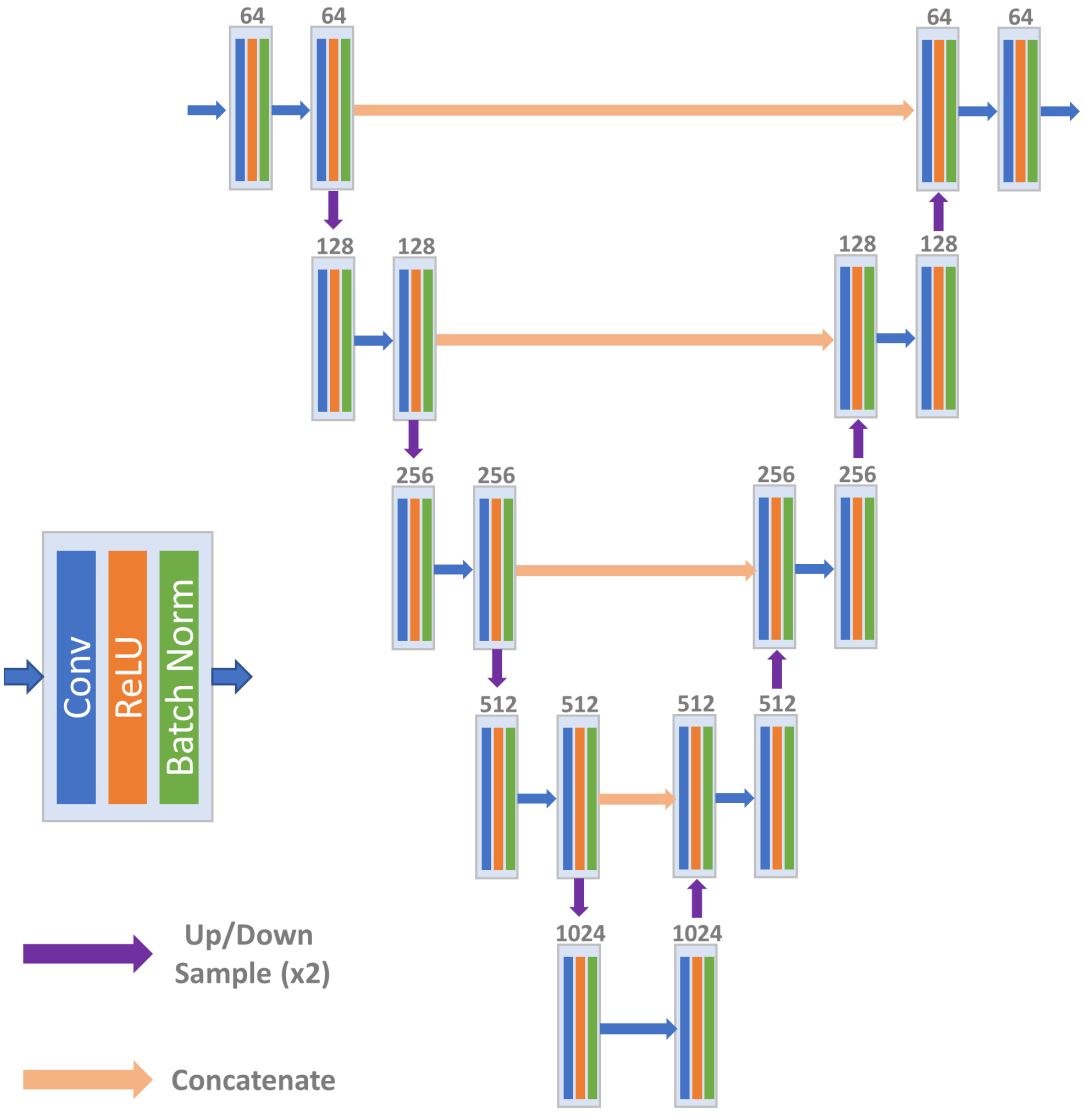

Figure 3.1. U-Net structure.

Each convolutional block consists of a 3D convolution layer (kernel $\mathbf{3 \times 3 \times 3}$*), a ReLU activation and a Batch Normalization layer. The number of output features are denoted above each block. Max pooling is used for down-sampling.*

The network was trained on 20 healthy subjects, where for each subject the 3D

volumetric local field map (matrix size $512 \times 512 \times 60$) was used as the input of the network. The ground truth label was chosen as the QSM of the same subject. We employed a patch-based approach and extracted 4199 patches (patch size $128 \times 128 \times 24$) from those 20 cases. The target QSM was reconstructed using MEDI. The training/validation/test split was 0.7/0.1/0.2. The L_1-norm of the difference map between output QSM and the ground truth was chosen as the training loss. The Adam optimizer (learning rate 0.001, max epoch 80) was employed for optimizing the loss during training. This work was implemented on a platform with Core i7 CPU, 128GB memory and 4 GTX TITAN XP GPUs (12GB each). The network training and inference were programmed using TensorFlow and Python.

3.4.3 Iterative Reconstruction: MEDI+DL

The DL outcome, χ_ϕ estimated by the network, was plugged into Eq. 3.5 in the form of an L_2 regularization. We proposed a high-pass-filter as the linear transform E prior to the penalization, as implemented using convolution with a spherical kernel S: $E(\chi) = \chi - S * \chi$. This resulted in a penalization on the high frequency components of the difference $\chi - \chi_\phi$. The rationale was that since our neural network was patched-based, spatial variations beyond the extent of a single patch could not be captured by the network. Therefore, by high-pass-filtering the difference map, the regularization allowed smooth variation across the scope. The radius of S was chosen as 10 mm.

MEDI+DL (Eq. 3.5) was minimized using the Gauss Newton method and a conjugate

gradient solver. An L-curve (Figure 3.2) was used to determine the regularization strength $\lambda_2 = 0.03$, which is the maximum value that achieves a fidelity cost lower than MEDI. MEDI+DL was performed on the 4 healthy subjects excluded from the training set and on the 8 MS patients. For comparison, MEDI (Eq. 3.4) was performed with $\lambda_1 = 0.001$ and $\lambda_{\mathrm{CSF}} = 0.1$ (31). Both MEDI and MEDI+DL were performed in Matlab. The fidelity cost $\left\|w\left(e^{-if} - e^{-i(d*\chi)}\right)\right\|_2$ was calculated for MEDI, DL and MEDI+DL, respectively, and normalized by $\left\|we^{if}\right\|_2$.

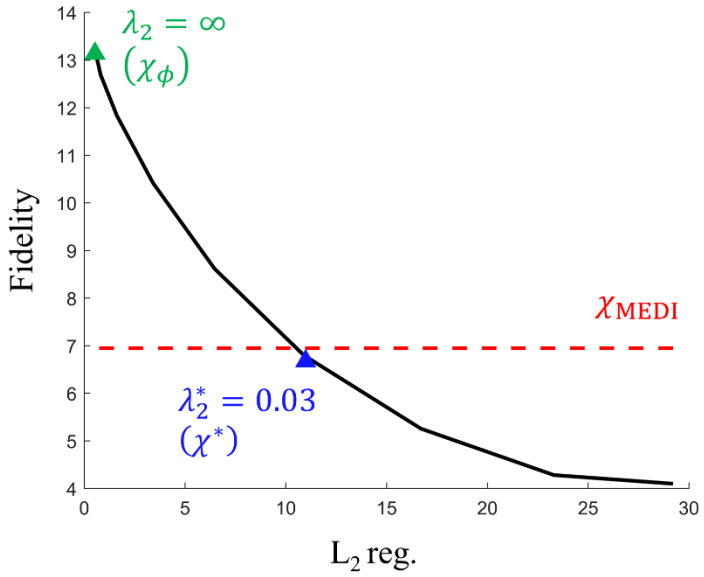

Figure 3.2. L-curve for choosing the regularization strength. $\boldsymbol{\lambda_2 = 0.03}$ *was picked (blue triangle) as the maximum value that gave a fidelity cost lower than that of MEDI (red dashed line). Note that* $\boldsymbol{\lambda_2 = \infty}$ *corresponded to a solution which was the same as the raw outcome from the network,* $\boldsymbol{\chi_\phi}$.

3.4.4 Quantitative Analysis

For both the healthy and MS subjects, three subcortical gray matter (SGM) regions, globus pallidus (GP), putamen (PU) and caudate nucleus (CN), were manually segmented, and the mean susceptibilities were measured within each segmented region. The susceptibilities of MS lesions were measured within manually drawn ROIs, and referenced to contralateral normal appearing white matter (NAWM) (2, 4). Agreement between the different methods was quantified using linear regression and Bland-Altman analysis.

3.5 Results

3.5.1 Healthy Subject

QSM reconstruction for one representative healthy subject is shown in Figure 3.3 (top row). As seen in the yellow boxes in Figure 3.3, veins were more distinct using MEDI+DL as compared to MEDI or DL. The same vessels were also discernable in the local field (Figure 3.3, left column).

The ROI measurements for SGM can be found in Figure 3.4a. Compared to MEDI, the average susceptibility suggested a difference of -5ppb (GP), 1ppb (PU), -5ppb (CN) for MEDI+DL, and -13ppb (GP), -4ppb (PU), -12ppb (CN) for DL. Compared to COSMOS, the relative susceptibility difference was -14% (GP), -30% (PU), 3% (CN) for MEDI, -23% (GP), -36% (PU), -20% (CN) for DL, and -17% (GP), -29% (PU), -7% (CN) for MEDI+DL.

Average reconstruction time was 95 seconds for MEDI, 2 seconds for DL, and 31 seconds for MEDI+DL (including time for generating χ_ϕ).

The average normalized fidelity cost was 0.73% for MEDI, 1.09% for DL and 0.68% for MEDI+DL.

3.5.2 Multiple Sclerosis Patient

QSM from one MS patient is shown in Figure 3.3 (bottom row). Veins close to the corpus callosum were better depicted using MEDI+DL, as compared to those using MEDI or DL.

ROI measurements of the SGM averaged over the 8 MS patients are shown in Figure 3.4b, indicating a difference of -23ppb (GP), -7ppb (PU), -15ppb (CN) for DL and -6ppb (GP), 3ppb (PU), -2ppb (CN) for MEDI+DL, compared to MEDI.

The linear regression result and Bland-Altman plot for MS lesion measurements are shown in Figure 3.5. The measurements between MEDI and MEDI+DL showed better correlation (R^2=0.81) than those between MEDI and DL ($R^2 = 0.62$). In addition, the Bland-Altman analysis indicated narrower limits of agreement [-16, 10] ppb between MEDI and MEDI+DL, as compared to [-27,13] ppb between MEDI and DL.

The average reconstruction time was 112 seconds for MEDI, 3 seconds for DL, and 38 seconds for MEDI+DL (including time for generating χ_ϕ).

The average normalized fidelity cost was 1.56% for MEDI, 1.84% for DL, and 1.55% for MEDI+DL.

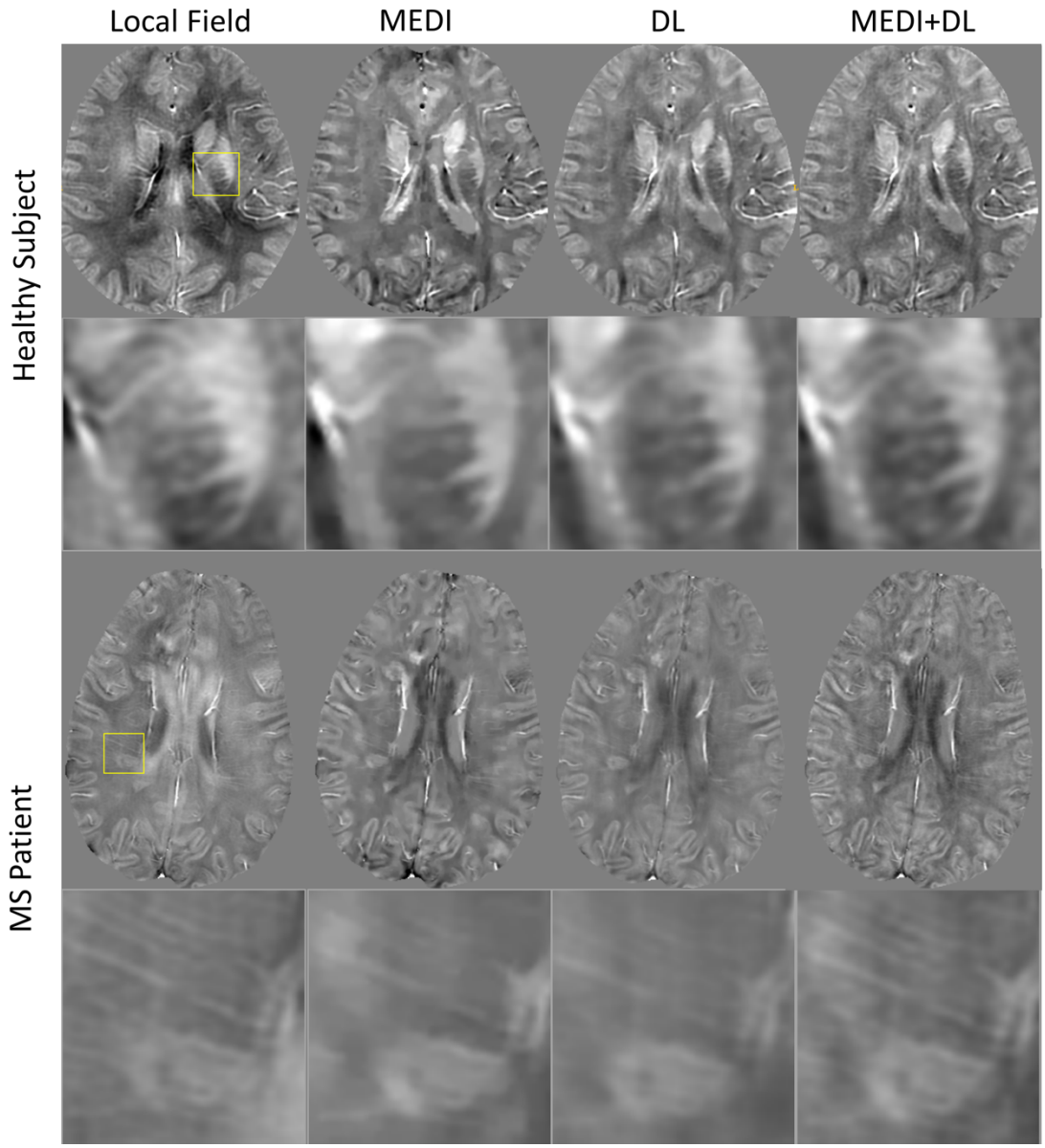

Figure 3.3. Example results of healthy subject and MS patient.

One axial slice from a healthy subject (top) and an MS patient (bottom). From left to right: local field, QSM reconstructed by MEDI, DL and MEDI+DL. MEDI+DL shows superior contrast of vein structures as compared to MEDI or DL, as indicated by the yellow boxed regions with zoomed image shown below each QSM. The structures are also present in the local field.

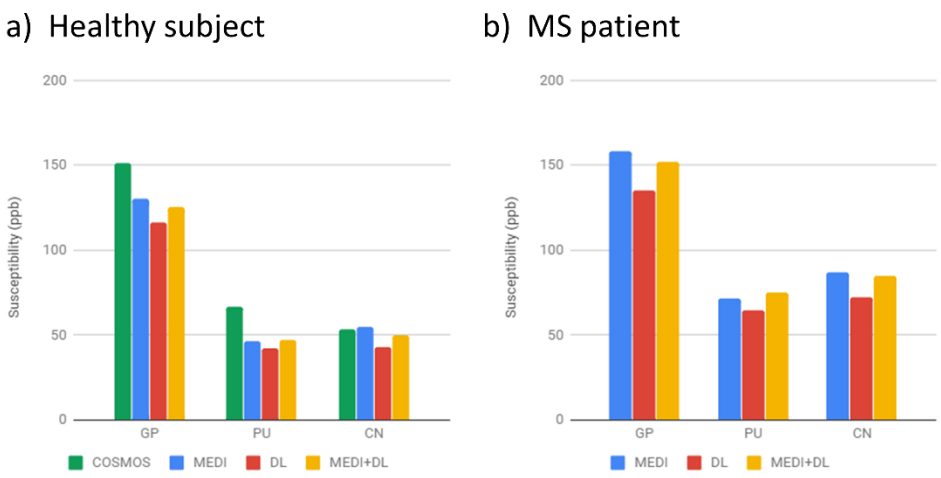

Figure 3.4. ROI measurement in healthy subject and MS patient.

Average ROI measurements of globus pallidus (GP), putamen(PU) and caudate nucleus (CN) on QSMs produced by MEDI, DL and MEDI+DL for healthy subjects (a) and MS patients (b). For healthy subjects, COSMOS measurements are also provided. Values shown are averaged over all subjects within each group. MEDI and MEDI+DL produce similar results, while DL under-estimates susceptibility compared to MEDI and MEDI+DL.

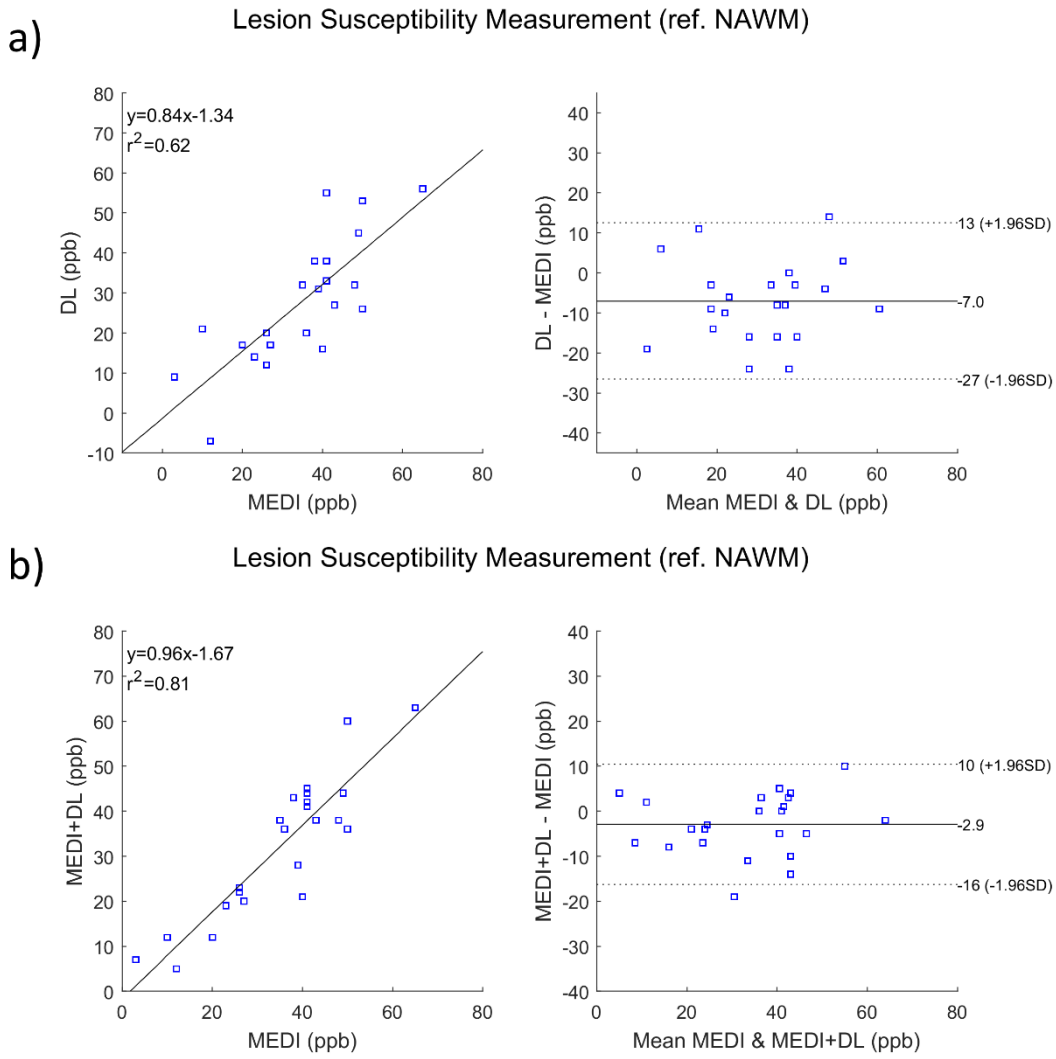

Figure 3.5. Scatter and Bland-Altman analysis for MS lesion measurement. Linear regression and Bland-Altman plots for MS lesion measurements for MEDI and DL (a) and MEDI and MEDI+DL (b). MEDI and MEDI+DL have a higher correlation, smaller bias and narrower limits of agreement. Each square represents a single lesion ROI measurement.

3.6 Discussion

Our data demonstrate that QSM reconstruction based on incorporating deep learning (DL) neural network output into Bayesian optimization reconstruction can provide superior contrasts and reduce fidelity cost compared to DL alone and traditional total variation regularized optimization. Our data also demonstrate that DL network outputs have a substantially larger fidelity cost, which can be reduced by imposing data fidelity through Bayesian optimization.

A traditional Bayesian QSM reconstruction consists of a fidelity term based on the measured data, and one or several regularization terms penalizing any deviation from prior knowledge about the susceptibility distribution. Typically, the regularization is expressed in L_1 and L_2 terms, which are known to have limitations. An L_2-regularization on the gradient promotes a smooth solution, and an L_1-regularization on the gradient, also known as the total variation, promotes a piece-wise linear or blocky solution. Consequently, the weighted total variation term, as used in MEDI (Eq. 3.4), may decrease visualization of subtle structures like small veins close to the corpus callosum (Figure 3.3). These limitations of traditional regularizations in Bayesian MRI reconstruction may be addressed with a deep convolution neural network based regularization (64, 65, 68, 69), as deep learning outperforms traditional methods in defining subtle image features. We employed the framework of deep learning plus Bayesian optimization in the QSM inverse problem, utilizing the neural network to produce an estimate of the susceptibility map and to guide the optimization by penalizing the L_2 difference between the solution and this network-estimated map. Our

proposed MEDI+DL produced better visualization of small veins compared to MEDI. Meanwhile, MEDI+DL took only ~30% of the time cost of MEDI, because the computationally expensive total variation in Eq. 3.4 was replaced with the L_2 regularization in Eq. 3.5.

Neural network based image processing is fast and can resolve complex non-linear mapping across domains, as demonstrated in denoising (70), super-resolution (71), segmentation (67) and reconstruction problems (62, 63, 72). Our current network employs architecture from QSMnet (63) and DeepQSM (62), where feed-forward 3D convolutional neural networks are used to perform the direct transform from tissue field to susceptibility map. However, in previous work (62, 63), the fidelity to the measured data was not considered. In this work, we evaluated the necessity of the fidelity by pairing the neural network with a fidelity cost in a numerical optimization framework (64, 65, 68). As demonstrated here, the fidelity cost for DL based solutions was much higher than that of MEDI, while MEDI+DL achieved a lower fidelity cost than that of MEDI.

Compared to COSMOS, a reasonable reference standard without regularization, DL substantially underestimated susceptibility, and MEDI+DL ameliorated this underestimation as demonstrated in our deep gray ROI measurements. MEDI+DL and MEDI provided similar susceptibility measurements in deep gray matter and in Multiple Sclerosis lesions. However, we observed that while MEDI+DL demonstrated less underestimation than MEDI in the putamen, there was greater underestimation in MEDI+DL as compared to MEDI in the globus pallidus and caudate nucleus. These

differences could be further investigated in future work.

Instead of training a cascading network to simulate a dedicated iterative projection process (64, 65), we simply used a pre-trained network to provide χ_ϕ and an iterative Gauss Newton algorithm to solve the target problem (Eq. 3.5). Potentially, the Gaussian distribution assumption (Eqs. 3.2&3.5) can be replaced with a stochastic collection of distributions, such as an aggregate of Gaussians from Monte-Carlo sampling a variational autoencoder-decoder (68), although this still involves an explicit form of L_2- or L_1-regularization, which forfeits the intrinsic benefit of deep learning. Future work should include more effective means to incorporate deep learning neural networks with traditional Bayesian optimization. One possible approach could be entirely removing the regularization term in Eq. 3.2 and embedding the CNN directly into the fidelity term as a preconditioning operator (73). This could exploit the full capacity of the CNN in characterizing the desired features in QSM as well as constraining the solution within the output manifold of the network.

3.7 Conclusion

This chapter presented a Bayesian method using a neural network to regularize the QSM inverse problem. The results showed quantitative consistency with a widely used total variation regularized method, and provided superior contrast of anatomical detail at less than half the computation cost.

CHAPTER 4

4 PRECONDITIONED TOTAL FIELD INVERSION

4.1 Abstract

In this chapter, we investigated systematic errors in traditional quantitative susceptibility mapping (QSM) with separating fitting of background field and local field. We developed a total field inversion (TFI) framework for QSM reconstruction to reduce these errors and improved QSM quality in the presence of severe susceptibility contrast through a numerical preconditioning technique.

4.2 Introduction

Traditional QSM procedure consists of two sequential stages (1): i) background field removal which extracts the local field generated by tissue from the total magnetic field, and ii) inversion from the local field to a distribution of tissue susceptibility. This enables a robust and efficient mapping of the midbrain area, particularly for iron-rich nuclei (1). However, several technical challenges remain.

A major challenge is inaccurate separation of background and local fields in previous background field removal methods, particularly near the region of interest (ROI) boundary where a large air-tissue susceptibility difference is present (1). Laplacian-based QSM methods have been proposed (25, 74-77) as attempts to bypass this separate fitting, based on the partial differential formulation of the forward signal equation (47, 78). However, the implementation of the Laplacian operator always

presents a trade-off between error suppression and the visualization of cortical brain tissue (79).

The presence of a large susceptibility dynamic range within the ROI is similarly a challenge in QSM, often leading to streaking artifacts (9, 18, 80-82). For instance, the susceptibility difference between intracerebral hemorrhage (ICH) and surrounding normal brain tissue can exceed 1 ppm (9). Recent work has focused on this challenge by separating the fitting processes for sources of strong (e.g. ICH) and weak (normal brain) susceptibilities, hence preventing ICH-related artifact from permeating into the normal brain (9, 80). However, these methods require carefully choosing the regularization strength (80) or threshold parameter (9) in detecting ICH.

In this chapter, we address both challenges using a unified framework, named total field inversion. We design a preconditioning numerical technique to enhance total field inversion in eliminating error propagation related to separate field fitting and in suppressing streaking artifacts in hemorrhage patient.

4.3 Theory

For QSM, the total magnetic field is typically decomposed into two components: the local field f_L defined as the magnetic field generated by the susceptibility χ_L inside a given ROI M (local susceptibility), and the background field f_B defined as the magnetic field generated by the susceptibility χ_B outside M (background susceptibility) (21):

$$f = f_B + f_L = d * (\chi_B + \chi_L) \qquad [4.1]$$

Here $*$ is the convolution operator, and d is the the field generated by a unit dipole with Lorentz sphere correction (83). The components f_B and f_L can be estimated separately: estimation of χ_B or f_B is referred to as background field removal. Various background field removal methods have been proposed, such as high-pass filtering (HPF)(84), projection onto dipole fields (PDF)(21) or Laplacian based methods (22, 23, 28). χ_L is then obtained from the local field $f_L = f - f_B$, typically using regularized inversion method (18, 26, 27, 33). This step is referred to as local field inversion (LFI). Errors from imperfect background field estimation propagate into the following local field estimation, ultimately producing errors in the tissue susceptibility χ_L. Although recent work (85) proposes to update the background field estimation during LFI, it demands a structural atlas to estimate the background susceptibility beforehand.

Here, we propose to estimate χ_B and χ_L jointly using a total field inversion (TFI) (30):

$$\chi^* = \underset{\chi}{\operatorname{argmin}} \frac{1}{2} \|w(f - d * \chi)\|_2^2 + \lambda \|M_G \nabla \chi\|_1, \qquad [4.2]$$

It employs the same linear formulation as the traditional QSM inversion problem (1, 27). Here $\chi = \chi_L + \chi_B$ represents the total susceptibility in the entire field of view. The data weighting w can be derived from the magnitude images (27).

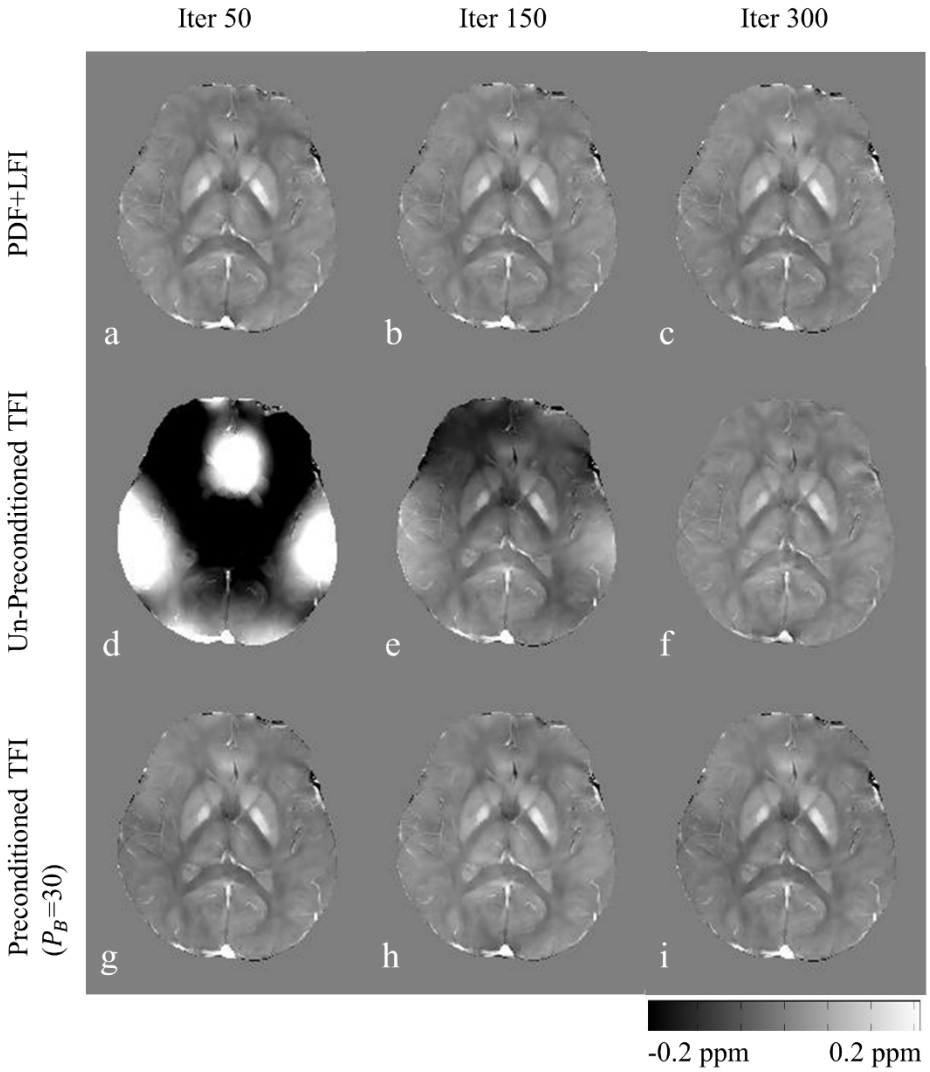

Figure 4.1. Brain QSM reconstructed by TFI with and without preconditioning.

Human brain QSM reconstructed using traditional PDF+LFI, un-preconditioned TFI and preconditioned TFI at different CG iterations. In order to produce a QSM similar to PDF+LFI with 50 iterations, TFI without preconditioning required 300 iterations. Preconditioning reduces this number down to 50.

The use of an iterative optimization solver, such as conjugate gradient (CG) (86), in solving Eq. 4.2 can lead to slow convergence compared to its LFI counterpart (27), as illustrated in a healthy brain in Figure 4.1. During early iterations, a portion of the background field is treated as local field, producing an artificial local susceptibility map (Figure 4.1d). To address this problem, we use prior-enhanced preconditioning (87) to improve CG convergence on Eq. 4.2. In (87), it is shown that if the solution χ is a Gaussian random vector with mean $\mathbf{0} \in \mathbb{R}^n$ and covariance matrix $\mathbf{\Gamma} \in \mathbb{R}^{n \times n}$, then a right-hand preconditioner P (see below) that approximates the covariance matrix $\mathbf{\Gamma}$, or $P^H P \approx \mathbf{\Gamma}$, will increase convergence speed. For TFI, a binary diagonal preconditioner P can be constructed as follows:

$$P(\boldsymbol{r}) = \begin{cases} 1, & r \in M \\ P_S, & \text{otherwise} \end{cases} \quad [4.3]$$

where $\boldsymbol{r}$ denotes the location for each voxel, M is the mask for tissue ROI and $P_S > 1$ which is empirically determined for each image content. If R2* map is available, one can also construct P as:

$$P(\boldsymbol{r}) = \begin{cases} 1, & r \in M \cap M_{R2^*} \\ P_S, & \text{otherwise} \end{cases} \quad [4.4]$$

where M_{R2^*} is the region with low R2* value ($M_{R2^*} \coloneqq R2^* < 30$ Hz) (30). The difference in those weights (1 vs. P_S) represents the contrast between weak susceptibility of soft tissues ($M \cap M_{R2^*}$) and relatively strong susceptibility sources including air, bone and hemorrhage.

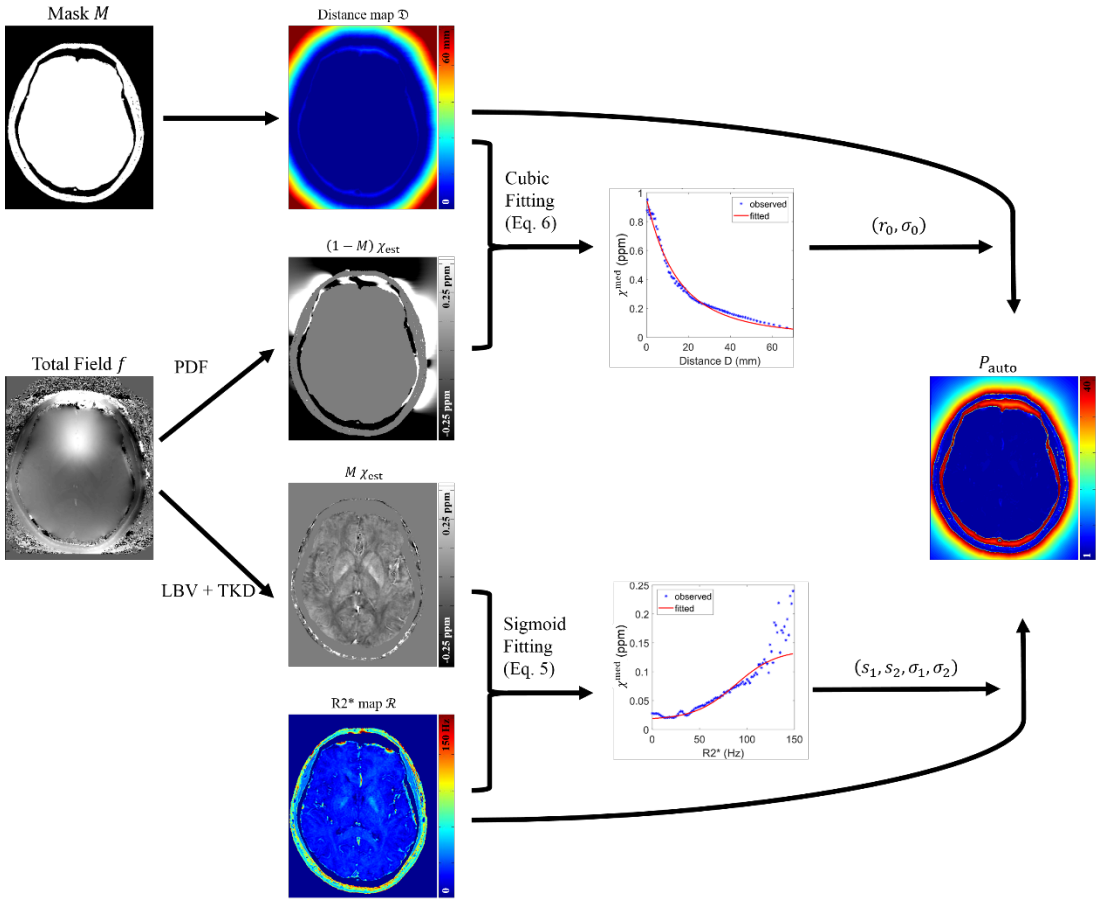

Figure 4.2. Flow chart for automatic generation of preconditioner.

The Preconditioner P_{auto} is generated from total field f and a soft tissue ROI mask M. Approximate susceptibility map χ_{est} was estimated using PDF and LBV+TKD for sources out- and inside M, respectively. Voxels outside M are grouped by their distance $\mathfrak{D}$ towards the boundary of M, and the median absolute susceptibility χ^{med} within each group was calculated and then fitted to a cubically decay function with respect to $\mathfrak{D}$. Voxels inside M are grouped by their R2 value $\mathcal{R}$ and the median absolute susceptibility χ^{med} within each group was calculated and then fitted to a sigmoid function with respect to $\mathcal{R}$. The fitted value for mean absolute susceptibility of*

each voxel was taken as the weight in the preconditioner P_{auto}.

In this chapter, we further propose a general procedure to construct P from the total field f, which extends the spatial distribution of P beyond the choice of a simple binary matrix and pre-determined weights. As illustrated in Figure 4.2, this procedure comes in two major steps:

Step 1: Solution estimation. This step generates an approximate susceptibility solution from the field input f. Susceptibility of strong source outside ROI M is estimated using PDF (21), while susceptibility source inside M is calculated using LBV (23) followed by Truncated K-space Division (TKD) (24). These two susceptibility components are then combined into a single map χ_{est}.

Step 2: Weight generation. Given the estimated solution χ_{est}, the absolute susceptibility value is used to construct the weight of a preconditioner that demonstrates the susceptibility level of each voxel. Considering that a single voxel in χ_{est} might contain noise and artifact, we group voxels with similar spatial or relaxational properties, depending where the voxels are relative to the ROI M, and calculate the median χ^{med} of absolute susceptibility values within each group: inside M, voxels are grouped by their R2* values $\mathcal{R}$. Each group is defined by a bin of 1-Hz width in R2* value. The calculated χ^{med} are then fitted to a sigmoid curve with respect to $\mathcal{R}$:

$$\chi^{\text{med}} \sim (\sigma_2 - \sigma_1)\frac{1}{1+e^{-(\mathcal{R}(r)-s_1)/s_2}} + \sigma_1 \qquad [4.5]$$

This is a soft threshold function, of which $[\sigma_1,\ \sigma_2]$ control the output range and $(s_1,\ s_2)$ control the shape; This is consistent with the prior knowledge that corresponding susceptibility and R2* values are expected to vary monotonically. Outside M, due to the absence of reliable R2* measurement, voxels are grouped by their distance $\mathcal{D}$ towards the boundary of the mask M. Each group is denoted by a bin of 1-mm width in $\mathcal{D}$ value. The calculated χ^{med} is then fitted to a cubic decay function with respect to $\mathcal{D}$:

$$\chi^{\text{med}} \sim \sigma_0 \left(1 + \frac{\mathcal{D}(\boldsymbol{r})}{r_0}\right)^{-3} \qquad [4.6]$$

where σ_0 and r_0 control its scale and decay rate, respectively. The final preconditioner P is then constructed as:

$$P(\boldsymbol{r}) = \begin{cases} \frac{\sigma_0}{\sigma_1}\left(1 + \frac{\mathcal{D}(\boldsymbol{r})}{r_0}\right)^{-3} & , \quad \boldsymbol{r} \notin M \\ \left(\frac{\sigma_2}{\sigma_1} - 1\right)\frac{1}{1+e^{-(\mathcal{R}(\boldsymbol{r})-s_1)/s_2}} + 1 & , \quad \boldsymbol{r} \in M \end{cases} \qquad [4.7]$$

Note that, consistent with the previous work (30), we scale P by σ_1 such that the weight for soft tissues (low R2*) is close to 1. The generated preconditioner P is provided to TFI (Eq. 4.2), which is solved using Gauss Newton method with conjugate gradient (CG) (26, 30).

4.4 Methods and Materials

We designed a numerical simulation to analyze the accuracy of the proposed TFI

approach in measuring susceptibility compared to conventional LFI. We also performed simulation experiment on examining the effect of automated preconditioner P_{auto} (Eq. 4.7) for healthy brain (non-ICH) and brain with intracerebral hemorrhage (ICH), compared with its empirical counterparts P_{emp} (Eq. 4.3) and $P_{\text{emp+R2*}}$ (Eq. 4.4). We finally compared their performance for in vivo brain QSM of both healthy subject and ICH patient.

4.4.1 Implementation Details

For P_{emp} (Eq. 4.3) and $P_{\text{emp+R2*}}$ (Eq. 4.4), the weight P_S was chosen as 30 for brain/head QSM (30). In estimating the approximate solution χ_{est}, PDF was performed with 5 CG iterations for sources outside M. For sources inside M, LBV was performed with a 3-voxel erosion of the ROI mask M to exclude noisy field measurement at the boundary, followed by TKD with a threshold of 0.2. At the weight generation stage, the nonlinear least squares fitting for parameters (σ_0, σ_1, σ_2, r_0, s_1, s_2) was performed using Matlab's fmincon routine. Distance map $\mathcal{D}$ was calculated using the method in (88). For brain/head QSM, $\lambda_1 = 0.001$ was used in Eq. 4.2. Susceptibility values were then referenced to the mean susceptibility within CSF. The Gauss Newton Conjugate Gradient (GNCG) solver was implemented as in (30), except for the choice of numerical conditioning parameter ϵ for calculating the weak derivative of L1-norm in Eq. 4.2: More specifically, $M_G \nabla P y$ was replaced with $\sqrt{|M_G \nabla P y|^2 + \epsilon}$ to avoid division by zero, see Appendix in (30). In (30), ϵ was chosen as 10^{-6} for all voxels. In this work, we chose $\epsilon = P^2 \times 10^{-6}$ such that the numerical conditioning weight would remain

approximately 10^{-6} for weak susceptibility tissue ($P \approx 1$) but increase for strong susceptibility sources ($P > 1$). This increased conditioning weight was intended for accelerating the GNCG solver (89).

4.4.2 Simulation

Accuracy of LFI and TFI. We constructed a numerical brain phantom of size $80 \times 80 \times 64$. Brain tissue susceptibilities were simplified to just 0 ppm, except for a single point susceptibility source of 0.1 ppm. Background susceptibilities were 0, and the total field was generated using Eq. 4.1. Both LFI and TFI without preconditioning (Eq. 4.2) were used, and the estimated value of the point source χ_S was compared to the truth χ_{ST} (0.1 ppm). For sequential inversion, both PDF (21) and LBV (75) were used for background field removal and MEDI (18) for local field inversion. This process was repeated by moving the point source within the entire ROI, resulting in an error map showing the spatial variation of the estimation error $|\chi_S - \chi_{ST}|/\chi_{ST}$ for each method, respectively. The regularization parameter λ was chosen as 10^{-3} for PDF+LFI, LBV+LFI and TFI.

Effect of the preconditioner P in TFI. A numerical head phantom of size 180×220×128 was constructed from Zubal phantom (90) with known susceptibilities simulating different brain tissues (44): white matter (WM) -0.046 ppm, gray matter (GM) 0.053 ppm, thalamus (TH) 0.073 ppm, caudate nucleus (CN) 0.093 ppm, putamen (PU) 0.093 ppm, globus pallidus (GP) 0.193 ppm, superior sagittal sinus (SSS) 0.27 ppm and cerebrospinal fluid (CSF) 0. Air (9 ppm), muscles (0 ppm) and

skull (-2 ppm) were distributed outside brain (Figure 4.4a). This phantom was then used to simulate two different scenarios: (A) non-ICH subject and (B) patient with intracerebral hemorrhage (ICH), which was represented by a spherical susceptibility source of 2ppm located inside the brain mask (Figure 4.5a). In both cases, the total field was computed from the true susceptibility map using the forward relation: $f = d * \chi$. Gaussian white noise (SNR=100) was added to this field. R2 was also simulated for each tissue type: WM 20 Hz, GM 20 Hz, TH 20 Hz, CN 30 Hz, PU 30 Hz, GP 45 Hz, SSS 45 Hz, CSF 4 Hz and ICH 100 Hz. For simplicity, R2 was used in place of R2* in the fitting of Eq. 4.5. During reconstruction, the root mean square error (RMSE) $\sqrt{\frac{1}{N}\sum_i \left(M\chi_i - M\chi_{\mathrm{T},i}\right)^2}$ between the estimated brain susceptibility $M\chi$ and the ground truth $M\chi_{\mathrm{T}}$, and the susceptibilities of CN and GP were calculated as metrics of reconstruction accuracy.

4.4.3 In Vivo Experiment: Healthy Head

5 healthy subjects were scanned at 3T (GE, Waukesha, WI) using multi-echo GRE with monopolar readout. Detailed imaging parameters were: FA = 15, FOV = 25.6 cm, TE1 = 5.0 ms, TR = 39 ms, #TE = 6, ΔTE = 4.6 ms, acquisition matrix = $512 \times 512 \times 144$, voxel size = $0.5 \times 0.5 \times 1$ mm3, BW = $\pm$62.5 kHz and a total scan time of 7 min. Scan was repeated at 5 different orientations for COSMOS reconstruction of brain QSM (66), with the brain mask generated by BET (91). At one orientation, total field is estimated from multi-echo GRE images (17) followed by graph-cut based phase unwrapping SPURS (19). ROI mask M for the entire head was

determined by thresholding the magnitude image I: $M := I > 0.15 \times I_{\max}$. R2* map was estimated using ARLO (92). TFI with different preconditioner choices P_{emp} (Eq. 4.3), $P_{\text{emp+R2*}}$ (Eq. 4.4) and P_{auto} (Eq. 4.7) were used to reconstruct the whole head QSM. Upon QSM reconstruction, the susceptibility of CN and GP were measured within manually drawn ROIs. The same measurement was also applied to COSMOS. Linear regression on brain tissue susceptibilities between TFI and COSMOS was conducted for each preconditioner choice, respectively.

4.4.4 In Vivo Experiment: ICH brain

5 patients with Intracerebral hemorrhage (ICH) were scanned at 3T (GE, Waukesha, WI) using multi-echo GRE with monopolar readout. Detailed imaging parameters are: FA = 15, FOV = 24 cm, TE1 = 4.5 ms, TR = 49 ms, #TE = 8, ΔTE = 5 ms, acquisition matrix = $512 \times 512 \times 64$, voxel size = $0.47 \times 0.47 \times 2$ mm3, BW = $\pm$62.5 kHz and a total scan time of 4 min. Total field is estimated from multi-echo GRE images followed by graph-cut based phase unwrapping (19). R2* map was calculated using ARLO (92). TFI with different preconditioner choices P_{emp} (Eq. 4.3), $P_{\text{emp+R2*}}$ (Eq. 4.4) and P_{auto} (Eq. 4.7) were used to reconstruct the QSM of the brain, with the brain ROI determined by BET. Upon QSM reconstruction, the susceptibility of CN and GP were measured using manually drawn ROIs. The mean susceptibility within a 5mm-wide layer surrounding the ICH site was computed for each QSM, respectively, to quantify the hypo-intense artifact around ICH (30).

4.5 Results

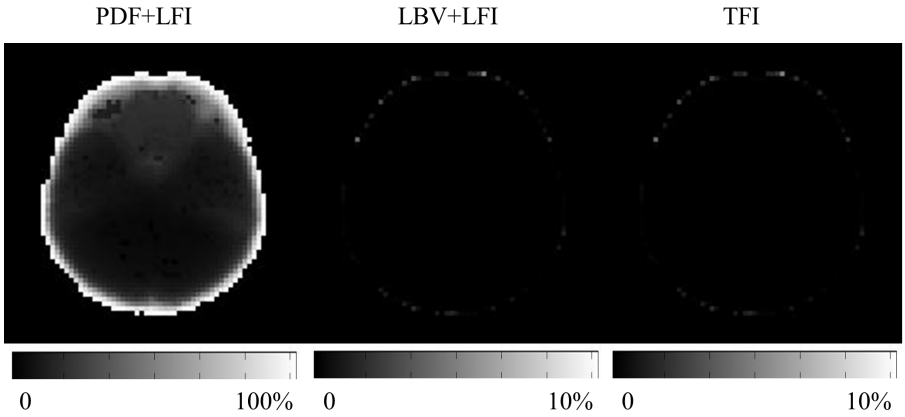

Figure 4.3. Error map for PDF+LFI, LBV+LFI and TFI in simulation.

Error map in estimating the 0.1ppm point source in simulation. When the point source is close to the ROI boundary, the error when using TFI is significantly smaller than that using PDF+LFI.

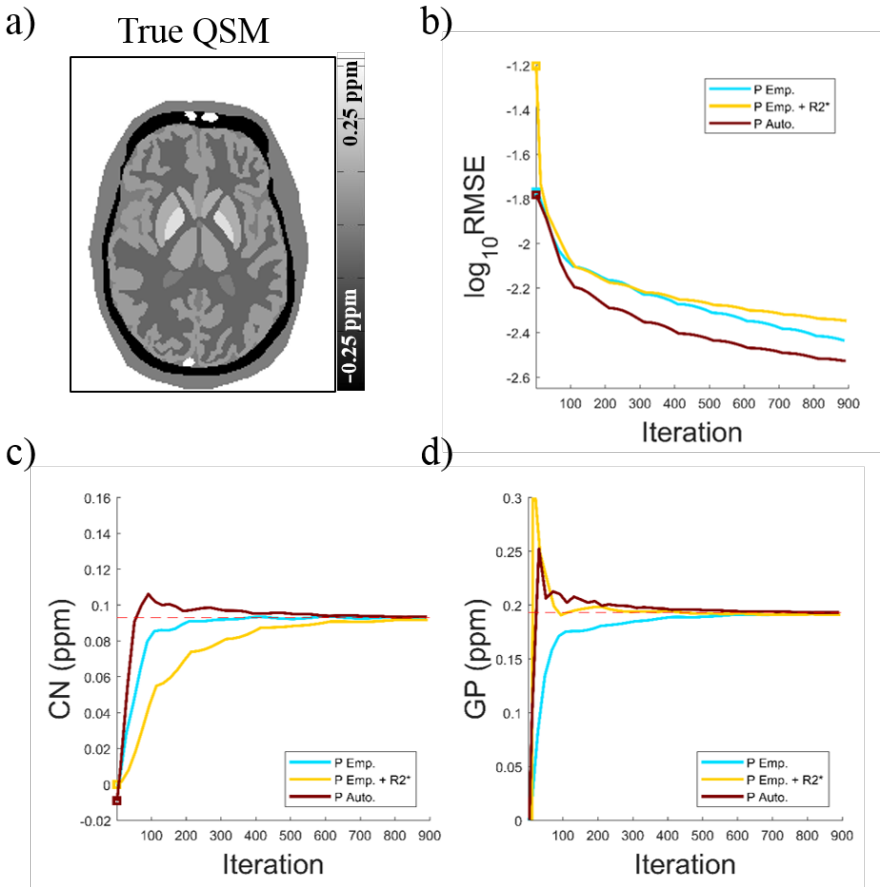

Figure 4.4. Simulation results for healthy scenario.

True susceptibility map χ_T (a), root-mean-square-error (RMSE) between the reconstructed and true QSM (b), ROI measurement for CN (c) and GP (d) at different CG iteration. P_{auto} achieved the lowest RMSE among three methods. Under-estimation of CN was consistently observed for P_{emp+R2^*} compared to P_{emp} and P_{auto}.

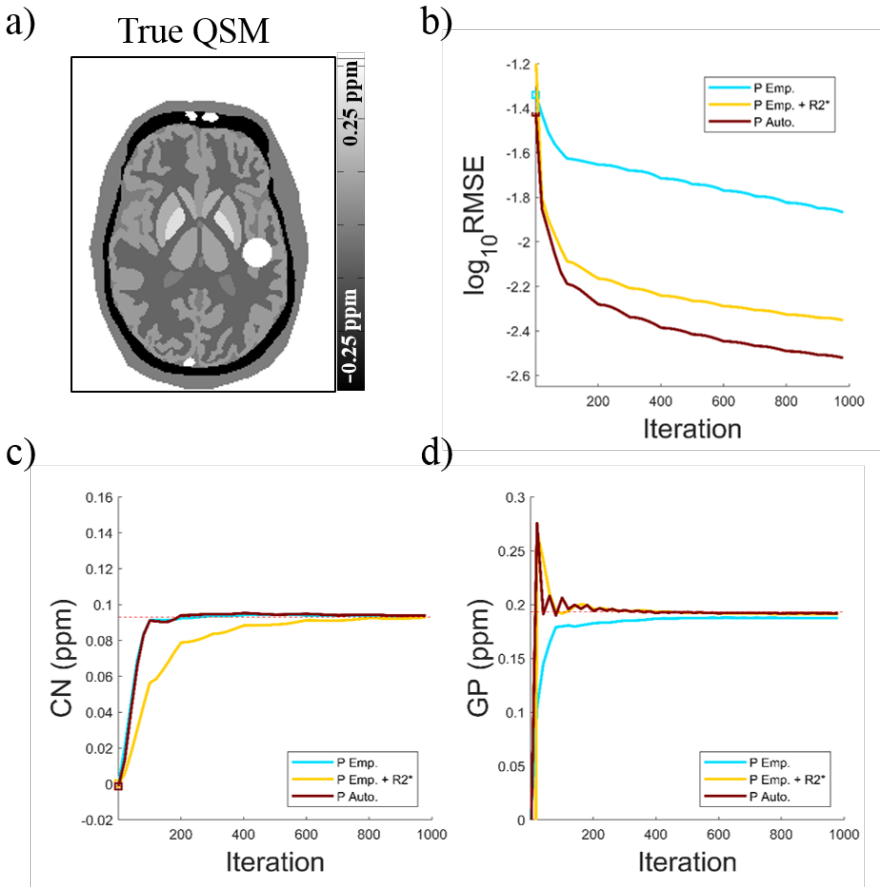

Figure 4.5. Simulation results for ICH scenario.

True susceptibility map χ_T (a), root-mean-square-error (RMSE) between the reconstructed and true QSM (b), ROI measurement for CN (c) and GP (d) at different CG iteration. P_{auto} achieved the lowest RMSE among three methods. At 1000th CG, P_{emp} has a much larger RMSE than those of P_{emp+R2^*} and P_{auto}. Under-estimation of CN was consistently observed for P_{emp+R2^*} compared to P_{emp} and P_{auto}. For GP measurement, P_{emp} showed a bias of -3% at 1000th CG, while the bias of P_{emp+R2^*} or P_{auto} was negligible.

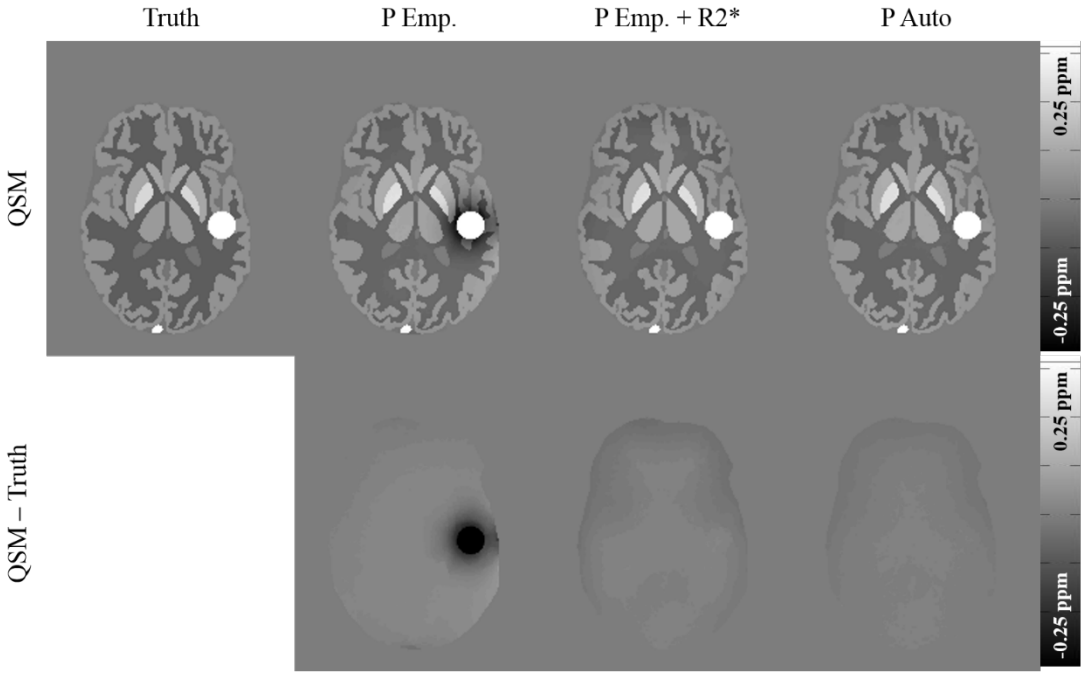

Figure 4.6. Simulation results for ICH scenario (image).

True brain QSM and brain QSM reconstructed by TFI using P_{emp}, P_{emp+R2^*} *and* P_{auto} *at the 1000th CG iteration (top row). Difference with respect to the true QSM was also shown (bottom row). Strong hypo-intense artifact around the ICH was present in* P_{emp} *result, leading to larger RMSE with respect to true brain susceptibilities shown in Figure 4.5b. This artifact over-shadowed part of the nearby GP.*

4.5.1 Simulation

Accuracy of LFI and TFI. In Figure 4.3, the PDF+LFI method demonstrated an estimation error of less than 10% at the central brain ROI; when the source was close within 4 voxels of the boundary, the error increased over 40%. In contrast, the

maximum error for both LBV+LFI and the proposed TFI were 4.8% throughout the ROI, including the boundary.

Effect of the preconditioner P in TFI. Results from non-ICH scenario were shown in Figure 4.4. All three preconditioner choices reached RMSE < 0.005 ppm at 1000 CG iterations, while P_{auto} achieved the lowest RMSE (Figure 4.4b). We compared the CG iteration number needed by each preconditioner in order to converge to $\pm 5\%$ range around the true value of each ROI: 170 (P_{emp}), 550 ($P_{\text{emp+R2*}}$) and 180 (P_{auto}) for CN (Figure 4.4c); 260 (P_{emp}), 70 ($P_{\text{emp+R2*}}$) and 170 (P_{auto}) for GP (Figure 4.4d).

Results from ICH scenario were shown in Figure 4.5. For ICH TFI, both $P_{\text{emp+R2*}}$ and P_{auto} reached RMSE < 0.005 ppm at 1000 CG iterations with lower RMSE for P_{auto}, while the RMSE using P_{emp} failed to go below 0.010 ppm (Figure 4.5b). This can be appreciated from the hypo-intense artifact around ICH in P_{emp} result at 1000 CG iterations (Figure 4.6). We compared the CG iteration number needed by each preconditioner in order to converge to $\pm 5\%$ range around the true value of each ROI: 90 (P_{emp}), 400 ($P_{\text{emp+R2*}}$) and 90 (P_{auto}) for CN (Figure 4.5c); 260 (P_{emp}), 100 ($P_{\text{emp+R2*}}$) and 110 (P_{auto}) for GP (Figure 4.5d).

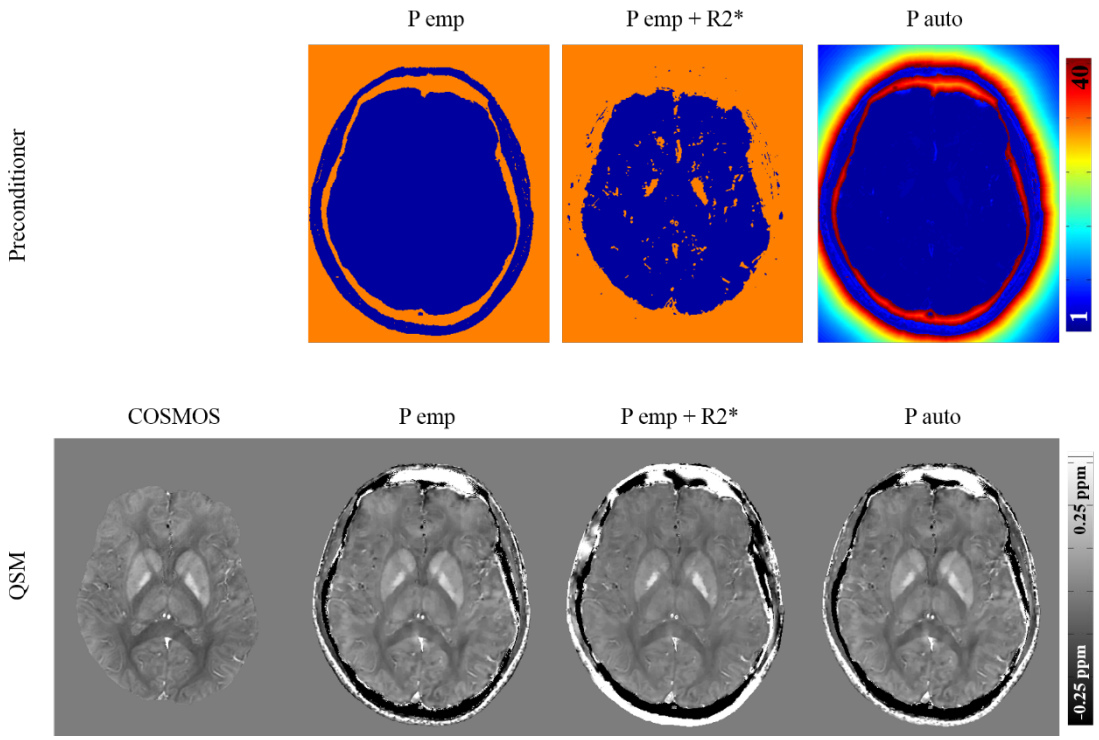

Figure 4.7. Example QSM of healthy subject with COSMOS. Top row: preconditioner maps of P_{emp}, P_{emp+R2^*} and P_{auto}. Bottom row: QSM for COSMOS, P_{emp}, P_{emp+R2^*} and P_{auto}. P_{emp} and P_{auto} obtain similar results for the entire head and comparable results with COSMOS for the brain. The contrast between CN and surrounding whiter matter is less distinct in P_{emp+R2^*} compared to other maps.

4.5.2 In Vivo Experiment: Healthy Head

Example of whole head TFI reconstruction of one healthy subject was shown in Figure 4.7. It was noted that with the R2* threshold (30 Hz) used in $P_{\text{emp+R2}^*}$, regions with

higher R2* such as GP were assigned the same weight ($P_S = 30$) as the background. In contrast, P_{auto} adaptively assigned weights to different regions according to their R2* values (Eq. 4.7). Figure 4.7 also showed the QSM reconstructed by COSMOS, TFI with P_{emp}, $P_{\text{emp+R2*}}$ and P_{auto}. P_{auto} obtained qualitatively comparable whole head QSM with P_{emp}, as well as a comparable brain QSM with COSMOS. Meanwhile, the gray/white matter contrast was less distinct in the $P_{\text{emp+R2*}}$ outcome, especially at the boundary of CN. This was confirmed by the CN susceptibility measurement for this subject: 0.058 ppm for COSMOS, 0.054 ppm for P_{emp}, 0.023 ppm for $P_{\text{emp+R2*}}$ and 0.050 ppm for P_{auto}. ROI measurement for CN and GP across all five healthy subjects indicates an averaged difference relative to COSMOS measurement were estimated: -5% (P_{emp}), -45% ($P_{\text{emp+R2*}}$) and -6% (P_{auto}) for CN; -9% (P_{emp}), -3% ($P_{\text{emp+R2*}}$) and -4% (P_{auto}) for GP. Linear regression of brain tissue susceptibilities between TFI and COSMOS showed a slope of 0.77 for P_{emp}, 0.67 for $P_{\text{emp+R2*}}$ and 0.76 for P_{auto} on average over five subjects.

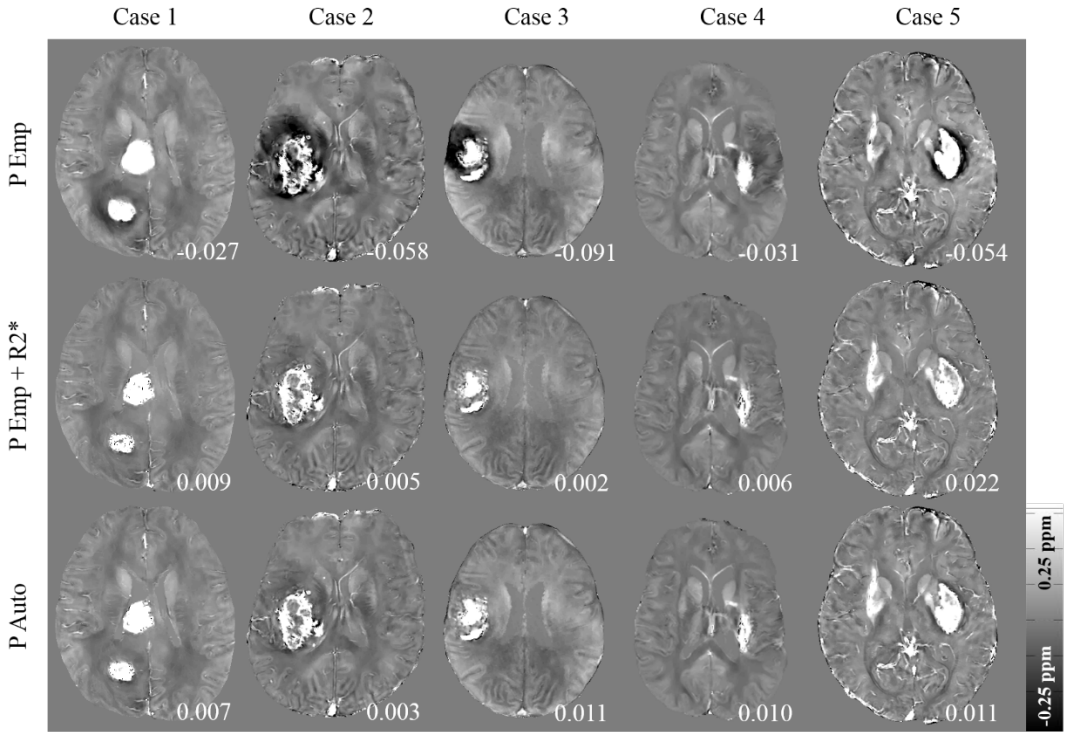

Figure 4.8. Example QSM of ICH patient.

Hypo-intense artifact was observed around ICH site in the output of P_{emp}*, while it was suppressed on both* $P_{emp+R_2^*}$ *and* P_{auto}*. Mean susceptibility value within a 5mm-wide layer outside the ICH was noted at the right-bottom corner of each map. The increase in this susceptibility measurement, as observed in* $P_{emp+R_2^*}$ *and* P_{auto} *compared to* P_{emp}*, reflected the reduced hypo-intense artifact.*

4.5.3 In Vivo Experiment: ICH brain

QSM for 5 ICH patients were shown in Figure 4.8. Hypo-intense artifact around ICH site present in P_{emp} outcome was reduced in those of $P_{\text{emp+R2}^*}$ and P_{auto}. The

mean susceptibility within a 5mm-wide layer surrounding the ICH site was noted at the corner of each QSM result, indicating an averaged increase of 0.061 ppm for $P_{\mathrm{emp+R2^*}}$ and 0.060 ppm for P_{auto}, compared to P_{emp}. However, $P_{\mathrm{emp+R2^*}}$ significantly under-estimated CN susceptibility compared to P_{emp} and P_{auto}: across 5 patients, the averaged CN measurement was 0.068 ppm for P_{emp}, 0.040 for $P_{\mathrm{emp+R2^*}}$ and 0.067 ppm for P_{auto}. Averaged GP measurement was 0.168 ppm for P_{emp}, 0.219 for $P_{\mathrm{emp+R2^*}}$ and 0.211 ppm for P_{auto}.

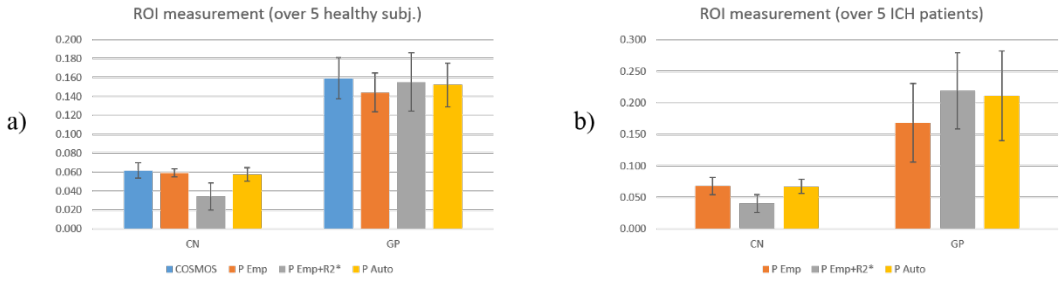

Figure 4.9. ROI measurement for healthy subject and ICH patient. Averaged measurements over 5 healthy subjects (left) and 5 ICH patients (right), respectively, for CN and GP. Underestimation was found in P_{emp+R2^*} in measuring CN, compared to P_{emp} and P_{auto}. For GP, P_{emp} gave significant under-estimation for GP in ICH patients compared to P_{auto} and P_{emp+R2^*}.

4.6 Discussion

In this work, we proposed a novel total field inversion approach for improved accuracy and convergence in QSM reconstruction. A numerical preconditioning technique was designed for the total field inversion process, where the preconditioner was determined using the total field input through a fully automated procedure, in contrast to the previous implementation (30) where a binary preconditioner with fix weights was empirically chosen and applied for all cases. It was shown that the proposed preconditioner achieves the lowest error metrics in numerical simulation. By incorporating the R2* information adaptively into the weights, the proposed preconditioner suppressed ICH-related artifact and preserved brain tissue contrast at the same time.

The sequential fitting of background field removal and LFI handles the same data using the same Maxwell's equations but demands arbitrary assumption or regularization (1) to differentiate the background field and the local field. For example, the inherit assumption in PDF is that the Hilbert space B spanned by all possible background unit dipole fields f_{dB} is orthogonal to the Hilbert space L spanned by all possible local unit dipole fields f_{dL} (21). However, this assumption breaks down when the local dipole source becomes close to the ROI boundary (21), thereby causing error in PDF. This was exemplified in our simulation result (Figure 4.3). Our proposed TFI eliminates this unnecessary separation as well as the associated error propagation. It is noted that LBV+LFI performed similarly with TFI, but requires an accurate ROI mask with high SNR phase measurement due to the lack

of an SNR weighting.

The development of preconditioning for accelerating conjugate gradient (CG) solver has been discussed in-depth throughout the literature of numerical optimization (86, 93). While traditional methods involve spectrum analysis of eigenvalues of the system matrix, direct application of such an approach to TFI reconstruction problem is challenging due to the huge problem size and the intrinsic convolution operation. Although recent work has shown that a preconditioner can be constructed in k-space to approximate the inverse of dipole kernel and gradient operator (94), its implementation for TFI is less prominent due to the presence of SNR weighting w and morphology constraint M_G in Eq. 4.2. Meanwhile, research has also been focused on developing preconditioner by leveraging prior information of the unknown solution, leading to a branch called prior-enhanced preconditioning (87, 95, 96). It relates the behavior of preconditioned CG to generalized Tikhonov regularization:

$$\arg\min_{\chi}\|A\chi - b\|_2^2 + \lambda_{\mathrm{Tik}}\|\Gamma\chi\|_2^2 \qquad [4.8]$$

The principle idea is that, one can construct a whitening operator Γ simulating the inverse covariance matrix Σ^{-1} by $\Gamma^{\mathrm{H}}\Gamma \approx \Sigma^{-1}$, if the prior distribution of χ is known as a Gaussian distribution $\chi \sim \mathcal{N}(0, \Sigma)$.

It has been shown (95, 96) that, if a preconditioner P is chosen such that $P^{-1} = \Gamma$, it can improve the solution of the following problem within limited CG iterations :

$$\chi = Py, \qquad y = \arg\min_{y}\|APy - b\|_2^2 \qquad [4.9]$$

This provides a guideline for choosing preconditioner P, that the transformed variable $P^{-1}\chi$ should have unit variance: $P^{-1}\chi \sim \mathcal{N}(0, I)$. In other words, P should be proportional to the presumed susceptibility magnitude of each voxel. By this guideline, a binary preconditioner was employed in the previous TFI work (30), in which an empirical weight, 30, was assigned to strong susceptibility sources such as air, bone and hemorrhage, whereas weight 1 was assigned to weak soft tissues. The current work enriches the preconditioner with more flexibilities in depicting the spatial distribution and dynamic contrast of the susceptibility map. It efficiently generates an approximated solution χ_{est} from the field input using PDF and LBV+TKD, and the absolute susceptibility value in χ_{est} was used in constructing the preconditioning weights. It is noted that, instead of directly using $|\chi_{\text{est}}|$ at each voxel, we group voxels by their spatial (distance towards object's boundary) or relaxational property (R2*), and calculate the median value of the observed absolute susceptibility value within each group. This approach aims to mitigate the influence of the noise and artifact in a single voxel, while median is chosen due to its robustness against extreme outliers.

R2* information is essential in our preconditioning technique, since it depicts the location of strong susceptibility tissues within the subject, such as ICH. As seen in simulation (Figure 4.6) and in vivo experiment (Figure 4.8), incorporation of R2* in the preconditioner ($P_{\text{emp+R2}^*}$ and P_{auto}) markedly suppressed the hypo-intense artifact surrounding the ICH site. Otherwise the QSM may suffer from qualitative and quantitative degradation, especially for structures close to ICH, as observed in the under-estimation of GP in Figure 4.5d. Previous work (30) employed a simple binary

threshold framework to differentiate weak/strong sources by their R2* and assigned the same weight to high-R2* regions as it did to the background. The proposed method incorporates R2* contrast into the construction of preconditioner in a more adaptive manner: It treats susceptibility χ_i at each voxel as a random variable dependent on the value of R2* value $\mathcal{R}$, with the conditional probability distribution $\mathcal{N}(0, \sigma^2(\mathcal{R}))$. Using $\sigma(\mathcal{R})$ as the preconditioning weight, $P^{-1}\chi$ presumably has unit variance. It is noted that if $\sigma_1 = 1,\ \sigma_2 = 30,\ s_1 = 30,\ s_2 \ll 1$, the sigmoid function (Eq. 4.5) reduces to the hard threshold used in $P_{\text{emp}+R2^*}$. Therefore, the proposed preconditioner can be thought as a generalized version of its empirical counterpart. Its scalability preserved the capability to suppress ICH-related artifacts (Figure 4.6 and Figure 4.8) and meanwhile addressed the under-estimation issue in the previous empirical choice $P_{\text{emp}+R2^*}$ for structures like CN.

The proposed automatic preconditioner construction method is readily applicable to QSM problem outside the head. The previous empirical choice (30) requires exhaustive search for preconditioning weights every time we move to new image contents, then an optimal combination of weights is determined and applied to similar objects. This is undesirable and unnecessary in the proposed method, which achieves lower reconstruction RMSE (Figure 4.4b and 4.5b) and reliable ROI measurement (Figure 4.9) without manual determination of the weights.

4.7 Conclusion

In this chapter, we propose a total field inversion (TFI) algorithm with automated

preconditioning for QSM reconstruction. It adjusts the preconditioner to the actual susceptibility content, improves convergence and produces reliable susceptibility measurement in various scenarios. This method adaptively incorporates the R2* contrast into the preconditioner, therefore suppresses ICH-related artifact and preserves normal tissue contrast at the same time.

CHAPTER 5

5 FUTURE DIRECTIONS AND CONCLUSION

5.1 Future Directions

Even though the techniques proposed in this work have significantly improved the accuracy, consistency and robustness of QSM reconstruction, there is still room for improvement upon the current methods. Future development areas may involve multi-contrast QSM reconstruction, body QSM application and direct QSM reconstruction from the complex MRI signal.

5.1.1 Multi-Contrast QSM

In the current preconditioned TFI approach in Chapter 4, The R2* information is needed to construct the preconditioner as in Eq. 4.7. If R2* is unavailable as in the case of single-echo acquisition, one can replace the sigmoid function in Eq. 4.7 with a simple uniform value which can be the median or mean over all absolute susceptibilities inside M, although an inferior ability to suppress ICH-related artifact is expected. A more sophisticated solution would be utilizing other image contrast such as T1w or T2w as the variant in Eq. 4.5 in place of R2*. In this way, we could complement the current preconditioned TFI with multiple image contrasts, which could be beneficial in single echo acquisition.

5.1.2 Body QSM

The preconditioning scheme proposed in Chapter 4 was designed for susceptibility

distribution with a large dynamic range. It could be potentially beneficial to addressing the severe contrast associated with the susceptibility distribution outside the brain. For example, a preconditioner could resolve susceptibility disparity between bone, thorax and soft tissue, thereby enabling a reliable and clean reconstruction of the carotid or chest QSM. Similarly, the preconditioned TFI might also benefit cardiac, musculoskeletal or animal QSM. Besides, the idea of automated zero reference (MEDI+0) in Chapter 2 could also be applied to body QSM applications, while other type of tissue such as subcutaneous fat might be targeted instead of CSF as a reference tissue (97).

5.1.3 Direct QSM from Complex MRI Image

As the extension for the TFI work, where the background field removal and local field inversion were combined, we could further incorporate the upstream operations (field estimation, phase unwrapping) into a unified step. This might be coined as direct QSM, denoting the QSM estimation directly from the multi-echo complex MRI images. The remaining challenges lie in the difficulties of providing a good initial guess for this non-convex and non-linear optimization process. Besides, the memory requirement is scaled linearly with the echo number. This could be problematic for high resolution QSM reconstruction with many echo times.

5.2 Conclusion

In this thesis, three major numerical techniques for improved quantitative susceptibility mapping in MRI are presented. In one method, delineation of the

cerebrospinal fluid (CSF) is provided in an automated manner and used to improve the consistency of CSF based zero reference in QSM normalization. In another approach, a deep learning model is incorporated with QSM reconstruction to achieve improved recovery of fine structures. Finally, a novel framework was introduced to QSM called preconditioning total field inversion. It not only enables a general inverse process that eliminates the error propagation associated with conventional QSM procedures, but also provides the means to extend current QSM applications towards different pathologies and applications where severe susceptibility contrasts are present.

APPENDIX

A. Derivation of Dipole Convolution

According to Maxwell's equations of static magnetism, a dipole magnetic moment $\boldsymbol{m}$ at origin ($\boldsymbol{r_0 = 0}$) generates a magnetic field $\widetilde{\boldsymbol{b}}(\boldsymbol{r})$ at location $\boldsymbol{r}$,

$$\widetilde{\boldsymbol{b}}(\boldsymbol{r}) = \frac{\mu_0}{4\pi} \frac{3(\boldsymbol{m}\cdot\hat{\boldsymbol{r}})\hat{\boldsymbol{r}}-\boldsymbol{m}}{r^3}\Big|_{r\neq 0} + \frac{2\mu_0}{3}\boldsymbol{m}\delta(r) \qquad [A.1]$$

where $\hat{\boldsymbol{r}}$ is the unit vector along the direction of $\boldsymbol{r}$. Therefore, the field perturbation generated by a distribution of magnetization $\boldsymbol{m}(\boldsymbol{r})$ could be denoted as convolution with Eq. A.1. However, in MRI signal acquisition, the non-overlapping between field generator and observer suggests that the second term in Eq. A.1 be dropped in the observed magnetic field. This is also referred to as the Lorentz correction. The corrected magnetic field $\boldsymbol{b}(\boldsymbol{r})$ (scaled to B_0) is,

$$\frac{\boldsymbol{b}(\boldsymbol{r})}{B_0} = \frac{\mu_0}{4\pi B_0} \int_{\boldsymbol{r}'\neq\boldsymbol{r}}^{\mathbb{R}^3} \frac{3\big(\boldsymbol{m}(\boldsymbol{r}')\cdot\hat{\boldsymbol{e}}_{\boldsymbol{r}\boldsymbol{r}'}\big)\hat{\boldsymbol{e}}_{\boldsymbol{r}\boldsymbol{r}'}-\boldsymbol{m}(\boldsymbol{r}')}{|\boldsymbol{r}-\boldsymbol{r}'|^3}\, d^3\boldsymbol{r}' = (\boldsymbol{d} * \chi) \qquad [A.2]$$

where the convolutional kernel is defined as,

$$\boldsymbol{d}(\boldsymbol{r},\boldsymbol{r}') = \frac{3\big(\hat{\boldsymbol{m}}(\boldsymbol{r}')\cdot\hat{\boldsymbol{e}}_{\boldsymbol{r}\boldsymbol{r}'}\big)\hat{\boldsymbol{e}}_{\boldsymbol{r}\boldsymbol{r}'}-\hat{\boldsymbol{m}}(\boldsymbol{r}')}{4\pi|\boldsymbol{r}-\boldsymbol{r}'|^3}\,, \quad \boldsymbol{r}\neq\boldsymbol{r}' \qquad [A.3]$$

Its z-component along the direction of the applied magnetic field $\boldsymbol{B_0}$ is referred to as the (scalar) dipole kernel,

$$d(\boldsymbol{r}) = \frac{1}{4\pi}\frac{3\cos^2\theta-1}{|\boldsymbol{r}|^3} \qquad [A.4]$$

giving the z-component of the observed magnetic field,

$$\frac{b(\boldsymbol{r})}{B_0} = d(\boldsymbol{r}) * \chi(\boldsymbol{r}) \qquad \text{[A.5]}$$

REFERENCE

1. Wang Y, Liu T. Quantitative susceptibility mapping (QSM): decoding MRI data for a tissue magnetic biomarker. Magnetic Resonance in Medicine 2015;73(1):82-101.
2. Chen W, Gauthier SA, Gupta A, Comunale J, Liu T, Wang S, Pei M, Pitt D, Wang Y. Quantitative susceptibility mapping of multiple sclerosis lesions at various ages. Radiology 2014;271(1):183-192.
3. Wisnieff C, Ramanan S, Olesik J, Gauthier S, Wang Y, Pitt D. Quantitative susceptibility mapping (QSM) of white matter multiple sclerosis lesions: interpreting positive susceptibility and the presence of iron. Magnetic resonance in medicine 2015;74(2):564-570.
4. Zhang Y, Gauthier SA, Gupta A, Chen W, Comunale J, Chiang GC-Y, Zhou D, Askin G, Zhu W, Pitt D. QSM and R2* measured changes during white matter lesion development in multiple sclerosis: myelin breaking down, myelin debris degradation and removal, and iron accumulation. AJNR American journal of neuroradiology 2016;37(9):1629.
5. Zhang S, Liu Z, Nguyen TD, Yao Y, Gupta A, Gauthier S, Wang Y. Automatic Cerebrospinal Fluid Zero Reference for Quantitative Susceptibility Mapping of Multiple Sclerosis. MULTIPLE SCLEROSIS JOURNAL: SAGE PUBLICATIONS LTD 1 OLIVERS YARD, 55 CITY ROAD, LONDON EC1Y 1SP, ENGLAND, 2018; p. 70-70.
6. Eskreis-Winkler S, Zhang Y, Zhang J, Liu Z, Dimov A, Gupta A, Wang Y. The clinical utility of QSM: disease diagnosis, medical management, and surgical planning. NMR in Biomedicine 2017;30(4).
7. Soman S, Bregni JA, Bilgic B, Nemec U, Fan AP, Liu Z, Barry RL, Du J, Main K, Yesavage J. Susceptibility-Based Neuroimaging: Standard Methods, Clinical Applications, and Future Directions. Current Radiology Reports 2017;5(3):11.
8. Wang Y, Spincemaille P, Liu Z, Dimov A, Deh K, Li J, Zhang Y, Yao Y, Gillen KM, Wilman AH, Gupta A, Tsiouris AJ, Kovanlikaya I, Chiang GC, Weinsaft JW, Tanenbaum L, Chen W, Zhu W, Chang S, Lou M, Kopell BH, Kaplitt MG, Devos D, Hirai T, Huang X, Korogi Y, Shtilbans A, Jahng GH, Pelletier D, Gauthier SA, Pitt D, Bush AI, Brittenham GM, Prince MR. Clinical quantitative susceptibility mapping (QSM): Biometal imaging and its emerging roles in patient care. J Magn Reson Imaging 2017;46(4):951-971. doi: 10.1002/jmri.25693
9. Sun H, Kate M, Gioia LC, Emery DJ, Butcher K, Wilman AH. Quantitative susceptibility mapping using a superposed dipole inversion method: Application to intracranial hemorrhage. Magnetic Resonance in Medicine 2015;DOI: 10.1002/mrm.25919.
10. Zhang J, Liu T, Gupta A, Spincemaille P, Nguyen TD, Wang Y. Quantitative mapping of cerebral metabolic rate of oxygen (CMRO2) using quantitative susceptibility mapping (QSM). Magnetic resonance in medicine 2015;74(4):945-952.
11. Chen W, Zhu W, Kovanlikaya I, Kovanlikaya A, Liu T, Wang S, Salustri C, Wang Y. Intracranial calcifications and hemorrhages: characterization with quantitative susceptibility mapping. Radiology 2014;270(2):496-505. doi:

10.1148/radiol.13122640
12. de Rochefort L, Nguyen T, Brown R, Spincemaille P, Choi G, Weinsaft J, Prince MR, Wang Y. In vivo quantification of contrast agent concentration using the induced magnetic field for time-resolved arterial input function measurement with MRI. Med Phys 2008;35(12):5328-5339.
13. Marques JP, Bowtell R. Application of a fourier-based method for rapid calculation of field inhomogeneity due to spatial variation of magnetic susceptibility. Concept Magn Reson B 2005;25B(1):65-78. doi: Doi 10.1002/Cmr.B.20034
14. Salomir R, De Senneville BD, Moonen CTW. A fast calculation method for magnetic field inhomogeneity due to an arbitrary distribution of bulk susceptibility. Concept Magn Reson B 2003;19B(1):26-34. doi: Doi 10.1002/Cmr.B.10083
15. Jackson JD. Classical eletrodynamics. 3rd ed: John Wiley and Sons, inc., 1999.
16. Haacke EM, Brown RW, Thompson MR, Venkatesan R. Magnetic Resonance Imaging - physical principles and sequence design. New York: Wiley-Liss, 1999.
17. Kressler B, de Rochefort L, Liu T, Spincemaille P, Jiang Q, Wang Y. Nonlinear regularization for per voxel estimation of magnetic susceptibility distributions from MRI field maps. IEEE transactions on medical imaging 2010;29(2):273-281. doi: 10.1109/TMI.2009.2023787
18. Liu T, Wisnieff C, Lou M, Chen W, Spincemaille P, Wang Y. Nonlinear formulation of the magnetic field to source relationship for robust quantitative susceptibility mapping. Magnetic Resonance in Medicine 2013;69(2):467-476. doi: 10.1002/mrm.24272
19. Dong J, Liu T, Chen F, Zhou D, Dimov A, Raj A, Cheng Q, Spincemaille P, Wang Y. Simultaneous Phase Unwrapping and Removal of Chemical Shift (SPURS) Using Graph Cuts: Application in Quantitative Susceptibility Mapping. Medical Imaging, IEEE Transactions on 2015;34(2):531-540.
20. Kee Y, Liu Z, Zhou L, Dimov A, Cho J, de Rochefort L, Seo JK, Wang Y. Quantitative Susceptibility Mapping (QSM) Algorithms: Mathematical Rationale and Computational Implementations. IEEE Transactions on Biomedical Engineering 2017.
21. Liu T, Khalidov I, de Rochefort L, Spincemaille P, Liu J, Tsiouris AJ, Wang Y. A novel background field removal method for MRI using projection onto dipole fields (PDF). NMR in biomedicine 2011;24(9):1129-1136.
22. Schweser F, Deistung A, Lehr BW, Reichenbach JR. Quantitative imaging of intrinsic magnetic tissue properties using MRI signal phase: An approach to in vivo brain iron metabolism? Neuroimage 2011;54(4):2789-2807. doi: http://dx.doi.org/10.1016/j.neuroimage.2010.10.070
23. Zhou D, Liu T, Spincemaille P, Wang Y. Background field removal by solving the Laplacian boundary value problem. NMR in biomedicine 2014;27(3):312-319. doi: 10.1002/nbm.3064
24. Shmueli K, de Zwart JA, van Gelderen P, Li TQ, Dodd SJ, Duyn JH. Magnetic susceptibility mapping of brain tissue in vivo using MRI phase data. Magnetic Resonance in Medicine 2009;62(6):1510-1522.

25. Bilgic B, Langkammer C, Wald LL, Setsompop K. Single-Step QSM with Fast Reconstruction. In Proceedings of the 3rd Internatinal Workshop on MRI Phase Contrast & Quantitative Susceptibility Mapping, Durham, NC. In Proceedings of the 3rd Internatinal Workshop on MRI Phase Contrast & Quantitative Susceptibility Mapping, Durham, NC, 20142014; p. 3321.
26. Liu J, Liu T, de Rochefort L, Ledoux J, Khalidov I, Chen W, Tsiouris AJ, Wisnieff C, Spincemaille P, Prince MR. Morphology enabled dipole inversion for quantitative susceptibility mapping using structural consistency between the magnitude image and the susceptibility map. Neuroimage 2012;59(3):2560-2568.
27. Liu T, Liu J, de Rochefort L, Spincemaille P, Khalidov I, Ledoux JR, Wang Y. Morphology enabled dipole inversion (MEDI) from a single-angle acquisition: Comparison with COSMOS in human brain imaging. Magnetic Resonance in Medicine 2011;66(3):777-783.
28. Sun H, Wilman AH. Background field removal using spherical mean value filtering and Tikhonov regularization. Magnetic Resonance in Medicine 2014;71(3):1151-1157.
29. Li W, Wang N, Yu F, Han H, Cao W, Romero R, Tantiwongkosi B, Duong TQ, Liu C. A method for estimating and removing streaking artifacts in quantitative susceptibility mapping. NeuroImage 2015;108:111-122.
30. Liu Z, Kee Y, Zhou D, Wang Y, Spincemaille P. Preconditioned total field inversion (TFI) method for quantitative susceptibility mapping. Magnetic resonance in medicine : official journal of the Society of Magnetic Resonance in Medicine / Society of Magnetic Resonance in Medicine 2017;78(1):303-315.
31. Liu Z, Spincemaille P, Yao Y, Zhang Y, Wang Y. MEDI+ 0: Morphology enabled dipole inversion with automatic uniform cerebrospinal fluid zero reference for quantitative susceptibility mapping. Magnetic Resonance in Medicine 2017.
32. Straub S, Schneider TM, Emmerich J, Freitag MT, Ziener CH, Schlemmer HP, Ladd ME, Laun FB. Suitable reference tissues for quantitative susceptibility mapping of the brain. Magnetic Resonance in Medicine 2016;DOI: 10.1002/mrm.26369. doi: 10.1002/mrm.26369
33. Bilgic B, Pfefferbaum A, Rohlfing T, Sullivan EV, Adalsteinsson E. MRI estimates of brain iron concentration in normal aging using quantitative susceptibility mapping. Neuroimage 2012;59(3):2625-2635.
34. Xu B, Liu T, Spincemaille P, Prince M, Wang Y. Flow compensated quantitative susceptibility mapping for venous oxygenation imaging. Magnetic resonance in medicine 2014;72(2):438-445.
35. Duyn JH, van Gelderen P, Li T-Q, de Zwart JA, Koretsky AP, Fukunaga M. High-field MRI of brain cortical substructure based on signal phase. Proceedings of the National Academy of Sciences 2007;104(28):11796-11801.
36. Choi JK, Park HS, Wang S, Wang Y, Seo JK. Inverse Problem in Quantitative Susceptibility Mapping. SIAM Journal on Imaging Sciences 2014;7(3):1669-1689.
37. Zhou L, Choi JK, Kee Y, Wang Y, Seo JK. Dipole incompatibility related artifacts in quantitative susceptibility mapping. arXiv preprint arXiv:170105457 2017.
38. Liu T, Xu W, Spincemaille P, Avestimehr A, Wang Y. Accuracy of the morphology enabled dipole inversion (MEDI) algorithm for quantitative

susceptibility mapping in MRI. IEEE transactions on medical imaging 2012;31(3):816-824.
39. Schweser F, Deistung A, Reichenbach JR. Foundations of MRI phase imaging and processing for Quantitative Susceptibility Mapping (QSM). Z Med Phys 2016;26(1):6-34. doi: 10.1016/j.zemedi.2015.10.002
40. Deistung A, Schweser F, Reichenbach JR. Overview of quantitative susceptibility mapping. NMR in Biomedicine 2017;30(4):DOI: 10.1002/nbm.3569. doi: 10.1002/nbm.3569
41. Haacke EM, Liu S, Buch S, Zheng W, Wu D, Ye Y. Quantitative susceptibility mapping: current status and future directions. Magn Reson Imaging 2015;33(1):1-25. doi: 10.1016/j.mri.2014.09.004
42. Wei H, Dibb R, Zhou Y, Sun Y, Xu J, Wang N, Liu C. Streaking artifact reduction for quantitative susceptibility mapping of sources with large dynamic range. NMR Biomed 2015;28(10):1294-1303. doi: 10.1002/nbm.3383
43. Sun H, Kate M, Gioia LC, Emery DJ, Butcher K, Wilman AH. Quantitative susceptibility mapping using a superposed dipole inversion method: Application to intracranial hemorrhage. Magn Reson Med 2016;76(3):781-791. doi: 10.1002/mrm.25919
44. Wisnieff C, Liu T, Spincemaille P, Wang S, Zhou D, Wang Y. Magnetic susceptibility anisotropy: cylindrical symmetry from macroscopically ordered anisotropic molecules and accuracy of MRI measurements using few orientations. Neuroimage 2013;70:363-376.
45. Li W, Wu B, Avram AV, Liu C. Magnetic susceptibility anisotropy of human brain in vivo and its molecular underpinnings. Neuroimage 2012;59(3):2088-2097.
46. Zhang Y, Gauthier SA, Gupta A, Comunale J, Chia-Yi Chiang G, Zhou D, Chen W, Giambrone AE, Zhu W, Wang Y. Longitudinal change in magnetic susceptibility of new enhanced multiple sclerosis (MS) lesions measured on serial quantitative susceptibility mapping (QSM). Journal of Magnetic Resonance Imaging 2016;DOI: 10.1002/jmri.25144. doi: 10.1002/jmri.25144
47. de Rochefort L, Liu T, Kressler B, Liu J, Spincemaille P, Lebon V, Wu J, Wang Y. Quantitative susceptibility map reconstruction from MR phase data using bayesian regularization: validation and application to brain imaging. Magnetic Resonance in Medicine 2010;63(1):194-206.
48. He X, Yablonskiy DA. Biophysical mechanisms of phase contrast in gradient echo MRI. Proceedings of the National Academy of Sciences 2009;106(32):13558-13563.
49. Luo J, He X, Yablonskiy D. Magnetic susceptibility induced white matter MR signal frequency shifts—experimental comparison between Lorentzian sphere and generalized Lorentzian approaches. Magnetic resonance in medicine 2014;71(3):1251-1263.
50. Lee J, Shmueli K, Fukunaga M, van Gelderen P, Merkle H, Silva AC, Duyn JH. Sensitivity of MRI resonance frequency to the orientation of brain tissue microstructure. Proceedings of the National Academy of Sciences 2010;107(11):5130-5135.
51. Liu C. Susceptibility tensor imaging. Magnetic resonance in medicine

2010;63(6):1471-1477.
52. Li X, Vikram DS, Lim IAL, Jones CK, Farrell JA, van Zijl PC. Mapping magnetic susceptibility anisotropies of white matter in vivo in the human brain at 7T. Neuroimage 2012;62(1):314-330.
53. Li X, Zijl P. Mean magnetic susceptibility regularized susceptibility tensor imaging (MMSR-STI) for estimating orientations of white matter fibers in human brain. Magnetic resonance in medicine 2014;72(3):610-619.
54. Lounila J, Ala-Korpela M, Jokisaari J, Savolainen M, Kesäniemi Y. Effects of orientational order and particle size on the NMR line positions of lipoproteins. Physical review letters 1994;72(25):4049.
55. Wharton S, Bowtell R. Fiber orientation-dependent white matter contrast in gradient echo MRI. Proceedings of the National Academy of Sciences 2012;109(45):18559-18564.
56. Wharton S, Bowtell R. Gradient echo based fiber orientation mapping using R2* and frequency difference measurements. Neuroimage 2013;83:1011-1023.
57. Wharton S, Bowtell R. Effects of white matter microstructure on phase and susceptibility maps. Magnetic resonance in medicine 2015;73(3):1258-1269.
58. Aggarwal M, Kageyama Y, Li X, Van Zijl PC. B0-orientation dependent magnetic susceptibility-induced white matter contrast in the human brainstem at 11.7 T. Magnetic resonance in medicine 2016;75(6):2455-2463.
59. Sukstanskii AL, Yablonskiy DA. On the role of neuronal magnetic susceptibility and structure symmetry on gradient echo MR signal formation. Magnetic resonance in medicine 2014;71(1):345-353.
60. Liu T, Eskreis-Winkler S, Schweitzer AD, Chen W, Kaplitt MG, Tsiouris AJ, Wang Y. Improved subthalamic nucleus depiction with quantitative susceptibility mapping. Radiology 2013;269(1):216-223.
61. Fan AP, Bilgic B, Gagnon L, Witzel T, Bhat H, Rosen BR, Adalsteinsson E. Quantitative oxygenation venography from MRI phase. Magn Reson Med 2013;10.1002/mrm.24918. doi: 10.1002/mrm.24918
62. Rasmussen KGB, Kristensen MJ, Blendal RG, Ostergaard LR, Plocharski M, O'Brien K, Langkammer C, Janke A, Barth M, Bollmann S. DeepQSM-Using Deep Learning to Solve the Dipole Inversion for MRI Susceptibility Mapping. Biorxiv 2018:278036.
63. Yoon J, Gong E, Chatnuntawech I, Bilgic B, Lee J, Jung W, Ko J, Jung H, Setsompop K, Zaharchuk G. Quantitative susceptibility mapping using deep neural network: QSMnet. NeuroImage 2018.
64. Schlemper J, Caballero J, Hajnal JV, Price AN, Rueckert D. A deep cascade of convolutional neural networks for dynamic MR image reconstruction. IEEE transactions on medical imaging 2018;37(2):491-503.
65. Aggarwal HK, Mani MP, Jacob M. Model based image reconstruction using deep learned priors (MODL). Biomedical Imaging (ISBI 2018), 2018 IEEE 15th International Symposium on: IEEE, 2018; p. 671-674.
66. Liu T, Spincemaille P, de Rochefort L, Kressler B, Wang Y. Calculation of susceptibility through multiple orientation sampling (COSMOS): a method for conditioning the inverse problem from measured magnetic field map to

susceptibility source image in MRI. Magnetic Resonance in Medicine 2009;61(1):196-204.
67. Ronneberger O, Fischer P, Brox T. U-net: Convolutional networks for biomedical image segmentation. International Conference on Medical image computing and computer-assisted intervention: Springer, 2015; p. 234-241.
68. Tezcan KC, Baumgartner CF, Konukoglu E. MR image reconstruction using deep density priors. arXiv 2017:arXiv: 1711.11386.
69. Wang G, Ye JC, Mueller K, Fessler JA. Image Reconstruction is a New Frontier of Machine Learning. IEEE transactions on medical imaging 2018;37(6):1289-1296.
70. Xie J, Xu L, Chen E. Image denoising and inpainting with deep neural networks. Advances in neural information processing systems2012; p. 341-349.
71. Dong C, Loy CC, He K, Tang X. Learning a deep convolutional network for image super-resolution. European conference on computer vision: Springer, 2014; p. 184-199.
72. Yang Y, Sun J, Li H, Xu Z. ADMM-Net: A deep learning approach for compressive sensing MRI. arXiv preprint arXiv:170506869 2017.
73. Ulyanov D, Vedaldi A, Lempitsky V. Deep image prior. arXiv preprint arXiv:171110925 2017.
74. Bredies K, Ropele S, Poser BA, Barth M, Langkammer C. Single-Step Quantitative Susceptibility Mapping using Total Generalized Variation and 3D EPI. In Proceedings of the 24th Annual Meeting ISMRM, Milan, Italy. In Proceedings of the 24th Annual Meeting ISMRM, Milan, Italy, 20142014; p. 3321.
75. Liu T, Zhou D, Spincemaille P, Wang Y. Differential approach to quantitative susceptibility mapping without background field removal. In Proceedings of the 22th Annual Meeting ISMRM, Milan, Italy. In Proceedings of the 22th Annual Meeting ISMRM, Milan, Italy, 20142014; p. 0597.
76. Sharma SD, Hernando D, Horng DE, Reeder SB. A joint background field removal and dipole deconvolution approach for quantitative susceptibility mapping in the liver. In Proceedings of the 24th Annual Meeting ISMRM, Milan, Italy. In Proceedings of the 24th Annual Meeting ISMRM, Milan, Italy, 20142014; p. 3321.
77. Langkammer C, Bredies K, Poser BA, Barth M, Reishofer G, Fan AP, Bilgic B, Fazekas F, Mainero C, Ropele S. Fast quantitative susceptibility mapping using 3D EPI and total generalized variation. NeuroImage 2015;111:622-630.
78. de Rochefort L, Nguyen T, Brown R, Spincemaille P, Choi G, Weinsaft J, Prince MR, Wang Y. In vivo quantification of contrast agent concentration using the induced magnetic field for time-resolved arterial input function measurement with MRI. Medical physics 2008;35(12):5328-5339.
79. Wu B, Li W, Guidon A, Liu C. Whole brain susceptibility mapping using compressed sensing. Magnetic Resonance in Medicine 2012;67(1):137-147. doi: 10.1002/mrm.23000
80. Wei H, Dibb R, Zhou Y, Sun Y, Xu J, Wang N, Liu C. Streaking artifact reduction for quantitative susceptibility mapping of sources with large dynamic range. NMR in Biomedicine 2015;28(10):1294-1303.

81. Buch S, Liu S, Ye Y, Cheng YCN, Neelavalli J, Haacke EM. Susceptibility mapping of air, bone, and calcium in the head. Magnetic Resonance in Medicine 2015;73(6):2185-2194.
82. de Rochefort L, Brown R, Prince MR, Wang Y. Quantitative MR susceptibility mapping using piece-wise constant regularized inversion of the magnetic field. Magnetic Resonance in Medicine 2008;60(4):1003-1009.
83. Li L, Leigh JS. Quantifying arbitrary magnetic susceptibility distributions with MR. Magnetic Resonance in Medicine 2004;51(5):1077-1082.
84. Haacke EM, Xu Y, Cheng YCN, Reichenbach JR. Susceptibility weighted imaging (SWI). Magnetic Resonance in Medicine 2004;52(3):612-618.
85. Poynton CB, Jenkinson M, Adalsteinsson E, Sullivan EV, Pfefferbaum A, Wells W. Quantitative Susceptibility Mapping by Inversion of a Perturbation Field Model: Correlation With Brain Iron in Normal Aging. Medical Imaging, IEEE Transactions on 2015;34(1):339-353.
86. Nocedal J, Wright S. Numerical optimization: Springer Science & Business Media, 2006.
87. Calvetti D, Somersalo E. Priorconditioners for linear systems. Inverse problems 2005;21(4):1397.
88. Mishchenko Y. A fast algorithm for computation of discrete Euclidean distance transform in three or more dimensions on vector processing architectures. Signal, Image and Video Processing 2015;9(1):19-27.
89. Kee Y, Deh K, Dimov A, Spincemaille P, Wang Y. Primal-dual and forward gradient implementation for quantitative susceptibility mapping. Magnetic Resonance in Medicine 2017. doi: 10.1002/mrm.26627
90. Zubal IG, Harrell CR, Smith EO, Rattner Z, Gindi G, Hoffer PB. Computerized three-dimensional segmented human anatomy. Medical physics 1994;21(2):299-302.
91. Jenkinson M, Pechaud M, Smith S. BET2: MR-based estimation of brain, skull and scalp surfaces. In Eleventh annual meeting of the organization for human brain mapping, Toronto, ON, 2015. Eleventh annual meeting of the organization for human brain mapping; p. 167.
92. Pei M, Nguyen TD, Thimmappa ND, Salustri C, Dong F, Cooper MA, Li J, Prince MR, Wang Y. Algorithm for fast monoexponential fitting based on Auto-Regression on Linear Operations (ARLO) of data. Magnetic Resonance in Medicine 2015;73(2):843-850. doi: 10.1002/mrm.25137
93. Hanke M, Nagy J, Plemmons R. Preconditioned iterative regularization. Numerical linear algebra 1993:141-163.
94. Bilgic B, Fan AP, Polimeni JR, Cauley SF, Bianciardi M, Adalsteinsson E, Wald LL, Setsompop K. Fast quantitative susceptibility mapping with L1-regularization and automatic parameter selection. Magnetic Resonance in Medicine 2014;72(5):1444-1459.
95. Calvetti D. Preconditioned iterative methods for linear discrete ill-posed problems from a Bayesian inversion perspective. Journal of computational and applied mathematics 2007;198(2):378-395.
96. Calvetti D, Pitolli F, Somersalo E, Vantaggi B. Bayes meets Krylov:

preconditioning CGLS for underdetermined systems. arXiv preprint arXiv:150306844 2015.
97. Sharma SD, Hernando D, Horng DE, Reeder SB. Quantitative susceptibility mapping in the abdomen as an imaging biomarker of hepatic iron overload. Magnetic Resonance in Medicine 2014;DOI: 10.1002/mrm.25448.